

Francesco Albicini

Numerical characterization of the hydrodynamic damping in a circular hydrofoil cascade

Masteroppgave i Mechanical Engineering

Veileder: Prof. Chirag Trivedi

Medveileder: PhD (c) Gabriele Gaiti

Januar 2024

Francesco Albicini

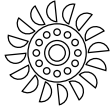
Numerical characterization of the hydrodynamic damping in a circular hydrofoil cascade

Masteroppgave i Mechanical Engineering
Veileder: Prof. Chirag Trivedi
Medveileder: PhD (c) Gabriele Gaiti
Januar 2024

Norges teknisk-naturvitenskapelige universitet
Fakultet for ingeniørvitenskap
Institutt for energi- og prosessteknikk



Kunnskap for en bedre verden



Abstract

The growing awareness of climate change and the related environmental impacts is driving a progressive transformation in the energy market, with an increasing relevance of the role of renewable energy sources. However, due to their intermittent and variable nature, challenges arise towards their integration into the current electrical grid. In this scenario, hydropower can be used to stabilize the system but this calls for an increased flexibility demanded to the power plants and all their components, especially the turbine.

Francis turbines are widely diffused in Norway, Italy and Europe in general, therefore there is significant interest in the understanding of how to operate these types of machines in today's and future energy scenario. Prior research at the Waterpower Laboratory (NTNU, Trondheim), mainly within the HydroCen framework, explored various aspects of structural and fluid dynamic phenomena across different turbine geometries. These researches provided a comprehensive overview of dynamic loads, stresses, deflections, and vibratory behaviour of the explored turbine systems.

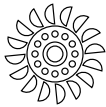
The primary objective of this master thesis is the characterization of the hydrodynamic damping of hydrofoils in a Circular Blade Cascade (CBC), consisting of eight of them in a radial symmetrical configuration. This specific setup has been devised to extend previous studies conducted on hydrofoils in non-cylindrical symmetry layouts. This study relies exclusively on numerical simulations and is a fundamental complement to the upcoming experimental campaign.

Firstly modal acoustic analysis has been carried out to assess natural frequencies and mode shapes of the structure. Fluid presence was found to lower natural frequencies compared to those in air, with minimal impact on eigenvectors. Subsequently, reverse one-way coupled simulations were per-

formed for various speeds, focusing on the first mode shape of the first two nodal diameters. Special attention was given to speeds close to lock-in. In this situation, a match occurs between the natural frequency of the structure and the vortex shedding frequency, potentially leading to catastrophic resonance effects. Using the “Aerodynamic Damping” tool in Ansys CFX[®], the damping work done by the fluid on the hydrofoils was calculated and then, following a “modal work approach”, the hydrodynamic damping value was derived.

The trend of the results aligns with previous experimental and numerical studies conducted in the Waterpower laboratory, demonstrating the almost independence of hydrodynamic damping from velocity pre-lock-in and a linear dependence post-lock-in. Not all the numerical values are, instead, convincing and consistent with previous studies due to the complex evaluation of some parameters.

In this context, the obtained values and trends will serve as a valuable benchmark for comparing future experimental results.



Sommario

Il cambiamento climatico ed i fenomeni ad esso correlati stanno progressivamente trasformando il mercato dell'energia, le fonti rinnovabili hanno assunto ed assumeranno un'importanza crescente. La loro natura intermittente e non programmabile pone, però, una sfida notevole alla loro integrazione nell'attuale rete di distribuzione elettrica. In questo scenario, l'idroelettrico può essere utilizzato per stabilizzare la rete, ma ciò implica una maggior richiesta di flessibilità agli impianti e a tutti i loro componenti, in particolare alla turbina.

Le turbine Francis sono ampiamente adottate in Norvegia, Italia e in Europa, vi è dunque un diffuso interesse nel comprendere come operare questi tipi di macchine nell'attuale e futuro scenario energetico. Studi precedentemente condotti presso il Waterpower Laboratory (NTNU, Trondheim), principalmente all'interno del progetto HydroCen, hanno indagato vari aspetti dei fenomeni strutturali e fluidodinamici su turbine di diversa geometria. Queste ricerche hanno fornito una panoramica completa sui carichi dinamici, sugli stress, e le deformazioni agenti sulle turbine analizzate, oltre che caratterizzarne il comportamento vibratorio.

L'obiettivo di questa tesi è caratterizzare lo smorzamento idrodinamico di un hydrofoil all'interno di una Circular Blade Cascade (CBC) composta da otto foil a semplice curvatura disposti radialmente in una configurazione assialsimmetrica. Questa specifica geometria è stata progettata con lo scopo di sviluppare gli studi precedenti, condotti su foil di uguale geometria ma organizzati in schiere lineari. Il lavoro svolto si basa esclusivamente su simulazioni numeriche e sarà un fondamentale strumento di supporto e validazione della futura campagna sperimentale.

Inizialmente si è eseguita un'analisi modale acustica al fine di valutare le fre-

quenze naturali e i modi di vibrare della struttura. La presenza dell'acqua riduce il valore delle frequenze naturali rispetto a quelle in aria, ma ha un minimo impatto sui modi di vibrare. Successivamente sono state effettuate delle simulazioni one-way FSI inverse per diverse velocità, concentrandosi sul primo modo di vibrare dei primi due diametri nodali. Particolare attenzione è stata posta sulle velocità vicine al lock-in. In questa situazione la frequenza naturale della struttura coincide con quella di vortex shedding e il sistema può entrare in risonanza, rischiando cedimenti catastrofici. Tramite l'utilizzo dello strumento "Aerodynamic Damping" in Ansys CFX[®], è stato possibile calcolare il lavoro di smorzamento fatto dal fluido sul foil e, successivamente, si è ricavato il valore dello smorzamento idrodinamico. Il trend dei risultati ottenuti è in linea con precedenti studi sperimentali e numerici condotti presso il Waterpower Laboratory e mostra la quasi totale indipendenza dello smorzamento idrodinamico dalla velocità prima del lock-in, e una sua dipendenza lineare dopo. Non tutti i valori numerici ottenuti sono però coerenti e convincenti a causa della difficile e talvolta arbitraria determinazione di alcuni parametri.

I valori ed i trend ottenuti saranno comunque un prezioso punto di riferimento per validare e confrontare i futuri risultati sperimentali.

Acknowledgments

Research work presented in the thesis is conducted in the [Waterpower Laboratory](#). The laboratory combines more than 100 years of experience in research and education. It has played leading roles in developing global hydropower, including efficient designs and implementation of turbines. The numerical simulations are carried out using [IDUN](#) computing cluster. The Idun cluster is a project between NTNU's faculties and the IT division that aims at providing a high-availability and professionally administrated computing platform for NTNU.

I would like to express my sincere gratitude to my supervisor at NTNU, Professor Chirag Trivedi, for accepting to be my advisor and allowing me to work on my thesis at the Waterpower Laboratory. This opportunity not only fulfilled my academic aspirations but also enabled me to embark on the Erasmus experience. I am also greatly thankful for his help and support throughout the thesis preparation process.

I would also like to thank my supervisor in Italy, Professor Anna Stoppato, for her unwavering support. Her guidance has been fundamental for organizing and structuring my thesis work and for navigating the challenges of studying abroad.

Special appreciation is owed to the PhD Gabriele Gaiti, who came to my rescue when struggling with unsuccessful simulations. His timely intervention redirected my focus and set me on the most promising path for achieving the desired results.

I extend my gratitude to all the people at the Vannkraftlaboratoriet: Professor Ole Gunnar Dahlhaug, PhD candidates, and all my colleagues in the office. The working environment that I found is truly spectacular—supportive, approachable, and friendly. I particularly want to thank PhD candidate Dadi

Dahal for all the help and the discussions about common challenges of our researchers and Emil Gjerde Dyb, for having shared with me the triumphs but especially the failures related to complex CFD simulations.

I want to express my heartfelt gratitude to all the people I met during my Erasmus experience; this incredible journey wouldn't have been the same without each of you. To all the friends from "Hammer", from Korsvika to gatherings at the cemetery in search of the Northern Lights, and the unforgettable moments in the Lofoten Islands, you have always been a safe place, a fantastic family at 2000km from home one can always rely on. Sharing these experiences with you has been an absolute pleasure, and I wish you all the best.

I am also truly grateful to all my lifelong and university friends: Federico, Matteo V., Matteo L., Enrico, Pietro, Sofia, Laura, Nimed, Lorenzo, Giada, Solimano, and Marco. Your friendship, warmth, type-two fun proposal and unwavering support, even when time and distance made it difficult, have been invaluable, especially in these intense last five years.

Finally, my deepest gratitude goes to Fabrizio, Cecilia and Chiara, my family. You have been a constant support for me, in all the aspects and challenges of my life. Thanks for your kindness, understanding and for having always believed in me. This thesis is dedicated to you.

Contents

Abstract	i
Sommario	iii
Acknowledgments	v
Contents	viii
List of tables	ix
List of figures	xii
Nomenclature	xiii
1 Introduction	1
1.1 Background	1
1.2 Challenges	2
1.3 Objectives	5
2 Literature review	7
3 Theory	9

3.1	Fluid structure interaction (FSI)	9
3.2	Dynamic loads on Francis turbines	11
3.3	Computational fluid dynamics	16
3.4	Structural mechanics	21
4	Methodology	33
4.1	Hydrodynamic damping	33
4.2	Modal acoustic simulation on Ansys Mechanical [®]	36
4.3	Reverse one-way simulation on Ansys CFX [®]	37
5	Results and discussions	39
5.1	Natural frequencies, mode shapes and kinetic energy	39
5.2	Work of the blade on the fluid W_D	42
5.3	Hydrodynamic damping ζ	44
5.4	Discussion	46
6	Conclusions	51
7	Future work	53
	References	54

List of tables

5.1	Natural frequencies of the first mode shape of each nodal diameter	39
5.2	Kinetic energy values and refereed maximum displacement for the first mode shape of each nodal diameter	42
5.3	Kinetic energy values refereed to a maximum displacement of $0.05mm$ for each nodal diameter	42
5.4	Work values W_D for each combination of nodal diameter and velocity	43
5.5	Hydrodynamic damping values for ND0 and ND1 as function of the velocity	44
5.6	Normalization factor for each nodal diameter	45
5.7	Hydrodynamic damping value for ND4 at $4m/s$	45

List of figures

1.1	Illustration of a hydropower plant and its components. Source: Waterpower Laboratory, NTNU	2
1.2	Efficiencies of the three principal types of hydraulic turbine as functions of the power specific speed, $\Omega_{sp} = \frac{\Omega\sqrt{P/\rho}}{(gH_E)^{5/4}}$, where P is the power delivered by the shaft, ρ is the density of water, H_E is the effective head at turbine entry, and Ω is the rotational speed in radiant per second	3
1.3	Variation of the filling grade of the water reservoir for energy production during the year. Source: Norwegian Water Resources and Energy Directorate	4
1.4	Application ranges for various types of hydraulic turbomachines, as a plot of Q versus H with lines of constant power determined assuming $\eta_0 = 0.8$	4
1.5	Circular Blade Cascade (CBC). Source: Waterpower Laboratory, NTNU	6
3.1	Solving algorithm for one-way coupling	10
3.2	Solving algorithm for two-way strong coupling	11
3.3	Vortex shedding on different scales	13
3.4	Vortex shedding regimes as a function of Re number	14
3.5	Tacoma Narrow Bridge collapsing, November 7, 1940	15

3.6	Time averaged $\bar{\phi}$ and fluctuating ϕ' description of a generic parameter ϕ for turbulent flow	19
3.7	S-N curve for a nonferrous alloy	22
3.8	MDOF system	24
3.9	Response of a free damped system to a step input as a function of the damping ratio	25
3.10	Transfer function amplitude depending on different values of damping ratio ζ	26
3.11	Hysteresis graph for a generic metallic material	28
4.1	Fluid particle moving on a vibrating structure	34
4.2	Modelled system for the modal acoustic analysis	36
4.3	Elements of the mesh adopted in the modal acoustic simulation. Each of them has 10 nodes with 3 DOF	37
4.4	Set up configuration for both steady and transient simulations. Two blades and two passages are modelled	38
5.1	Comparison between the first mode shape of nodal diameter 0 in air (a) and water (b)	40
5.2	Comparison between the first mode shape of nodal diameter 1 in air (a) and water (b)	41
5.3	Work done by the blade on the fluid for the first mode shape of ND0 and ND1	43
5.4	Hydrodynamic damping ζ for ND0 as function of the velocity	45
5.5	Hydrodynamic damping ζ for ND0 as function of the velocity	46
5.6	Numerical and experimental results found by Bergan C., Tengs E. et. al. for a single hydrofoil with a symmetric trailing edge	47
5.7	Comparison between ζ for ND0 and ND1	48

Nomenclature

Abbreviation

CBC	Circular blade cascade
CFD	Computational fluid dynamics
DNS	Direct numerical simulation
DOF	Direct numerical simulation
FEM	Finite element method
FSI	Fluid structure interaction
GHG	Green house gasses
HHF	High head Francis
HPC	High-performance computer
LES	Large eddy simulation
MDOF	Multiple degrees of freedom
ND	Nodal diameters
NS	Navier-Stokes equations
NTNU	Norwegian University of Science and Technology
RANS	Reynolds-averaged Navier-Stokes equation
RSI	Rotor stator interaction

RVR Rotating Vortex Rope
SDOF Single degree of freedom

Latin symbols

A Area (m^2)
 c Damping (kg s^{-1})
 \mathbf{C} Damping matrix (kg s^{-1})
 c_{cr} Critical damping (kg s^{-1})
 c_m Meridian component of absolute velocity (m s^{-1})
 c_u Tangential component of absolute velocity (m s^{-1})
 D Damage due fatigue phenomena
 d Depth, or thickness, of the water layer (m)
 F Force (N)
 f Frequency (Hz)
 g Gravity acceleration (m s^{-2})
 i Imaginary variable
 K Stiffness (N m^{-1})
 \mathbf{K} Stiffness matrix (N m^{-1})
 k Turbulent kinetic energy ($\text{m}^2 \text{s}^{-2}$)
 L Length (m)
 \vec{l} Load vector (N)
 \mathbf{M} Mass matrix (kg)
 M Mass (kg)
 N Maximum number of stress cycles
 n Number of stress cycles
 p Pressure (Pa)

\vec{p}_0	Load scaling vector (N)
\mathbf{R}	Coupling matrix (m^2)
s	Complex number
T	Time interval (s)
t	Time (s)
U	Total potential energy (J)
\vec{u}	Displacement vector (m)
u	Flow velocity (m s^{-1})
\vec{u}_0	Displacement scaling vector (m)
v	Peripheral velocity (m s^{-1})
W	Work (J)
w	Relative velocity (m s^{-1})
z	Number of blades/guide vanes

Dimensionless numbers

Re	Reynolds number
St	Strouhal number

Greek symbols

α	Angle between two consecutive alignments of guide and runner blades (rad)
ϵ	Rate of dissipation of turbulent kinetic energy ($\text{m}^2 \text{s}^{-3}$)
ε	Material deformation
ζ	Damping ratio
η_0	Efficiency
μ	Dynamic viscosity (Pa s)
ν	Kinematic viscosity ($\text{m}^2 \text{s}^{-1}$)

ρ	Density ($\text{m}^2 \text{s}^{-1}$)
σ	Normal stress (MPa)
τ	Tangential stress (MPa)
$\vec{\phi}$	Eigenvector (m)
Φ	Generic variable
ω	Angular speed (rad s^{-1})
Ω	Natural frequency of the structure in the fluid (rad s^{-1})
ω	Turbulence frequency (rad s^{-1})

Superscripts and subscripts

cr	Critical
D	Damping
F	Fluid
g	Guide vane
I	Impulse
i	Generic index
j	Generic index
K	Stiffness
n	Natural frequency
r	Runner vane
s	Vortex shedding
S	Structure
w	Water

Introduction

1.1 Background

Climate change and its associated phenomena represent one of the greatest challenges that, as humanity, we are called to face. Several aspects of our society have a significant impact on the climate, and among these, the emission of greenhouse gasses (GHG) associated with energy production is one of the predominant factors [1].

During the last decades, the development of humankind and the rapid widespread industrialization has caused a steady increase in the global primary energy consumption [2] and, consequently, in the production and emissions of GHG, especially CO₂ [3]. It is therefore crucial to adopt lifestyles and policies that are environmentally virtuous but, it is also fundamental and urgent to produce the energy we need in sustainable ways.

The increasing awareness of environmental issues is leading to a gradual shift in energy demand: a decline for hydrocarbons is expected in favour of renewable energy sources that, according to [4], could represent 65% of the primary energy by 2050. Most of them, such as solar and wind, are intermittent and not programmable meaning that the energy is not always available, as local variations in weather occur. From this perspective, hydroelectric power represents an anomaly because, thanks to the presence of reservoirs, it is possible to decide when to generate power and in which quantity.

This characteristic makes hydroelectric plants increasingly more important for the stabilization of the electrical grid, which, in the future, will experience a growing penetration of renewable and therefore, intermittent, energy sources. Performing this task may entail that the plant has to operate in off-design conditions and/or undergo frequent starts and stops. These types of

operations have a negative impact on the plant's operating life, availability and reliability. The elements of the plant, especially the turbine, are then subjected to stresses and wear for which they are not designed. Failures and maintenance operations can then be more frequent and onerous than expected.

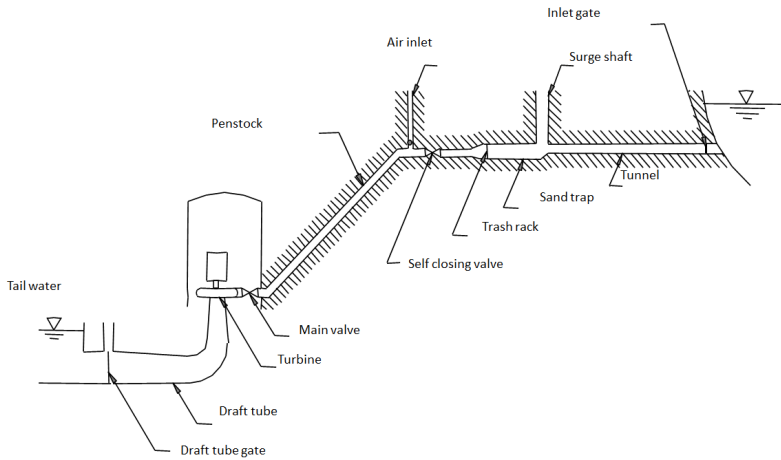


Figure 1.1: Illustration of a hydropower plant and its components. Source: Waterpower Laboratory, NTNU

1.2 Challenges

Hydropower is one of the earliest forms of energy harnessed by humanity. The earliest documented use of water wheels traces back to the 4th century BC in India [5]. While historically employed primarily for agricultural applications, the utilization of water wheels for electricity production began in the 19th century. The heart of a hydroelectric plant is the turbine that, connected to a generator, produces electric energy.

Nowadays three main types of turbines exist: Pelton, Francis, and Kaplan. Each of them is suited to different flow and head conditions and has characteristic efficiency curves. James B. Francis, the inventor of the Francis turbine, was able to obtain a hydraulic efficiency of 90% already in 1848 [6].

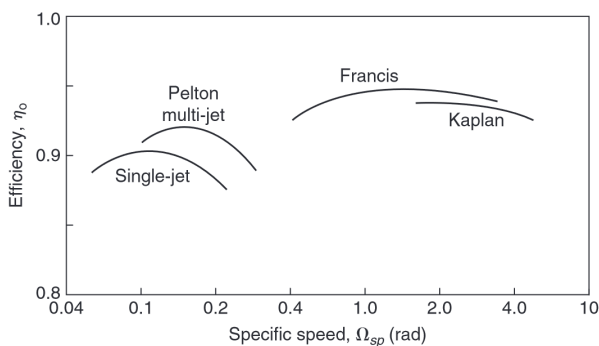


Figure 1.2: Efficiencies of the three principal types of hydraulic turbine as functions of the power specific speed, $\Omega_{sp} = \frac{\Omega \sqrt{P/\rho}}{(gH_E)^{3/4}}$, where P is the power delivered by the shaft, ρ is the density of water, H_E is the effective head at turbine entry, and Ω is the rotational speed in radiant per second [7]

As it is possible to observe in Figure 1.2, the Francis turbines have an efficiency curve relatively flat. This means that they can work in conditions different from the design ones still ensuring good performances. The necessity to operate the plant in an off-design state is due to different factors and their possible combinations, for example:

- needs to satisfy the load request of the grid;
- needs to balance the grid;
- hydrological conditions;
- seasonal and climatic conditions (Figure 1.3).

Francis turbines are the most widely adopted in Norway [8] since they fit quite well the characteristics of the territory. Over 50% of the country's land area is above 600 m [9] and the average annual precipitation is over 1100 mm. As it is possible to see in Figure 1.4, under these circumstances, Francis turbines are the most suitable, especially the High Head Francis turbine (HHF).

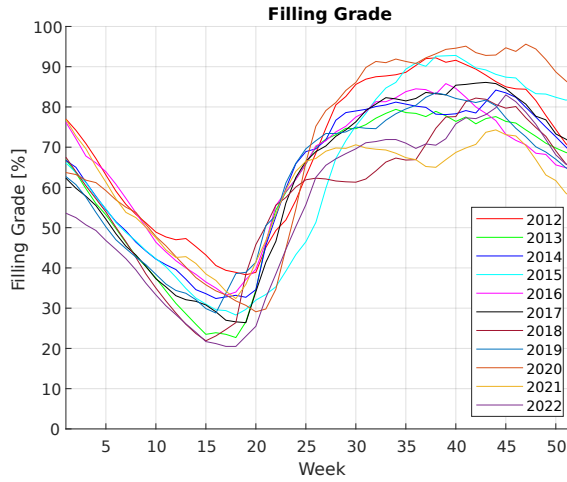


Figure 1.3: Variation of the filling grade of the water reservoir for energy production during the year. Source: Norwegian Water Resources and Energy Directorate

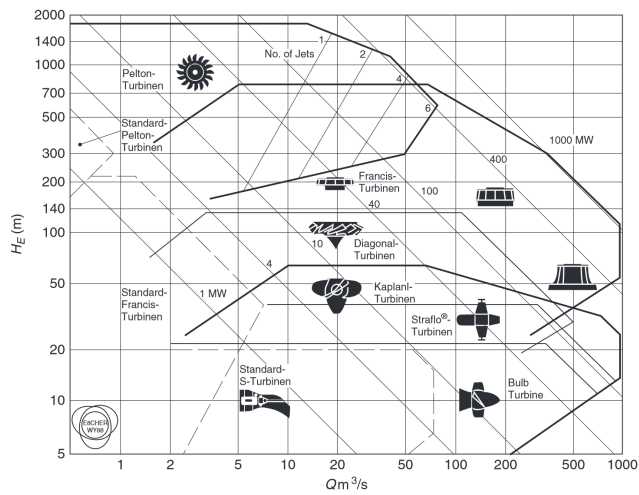


Figure 1.4: Application ranges for various types of hydraulic turbomachines, as a plot of Q versus H with lines of constant power determined assuming $\eta_0 = 0.8$ [7] (Courtesy Sulzer Hydro Ltd., Zurich)

The efficiency of this type of machine, remarkably high as early as 1848, has progressively enhanced over time through the integration of numerical tools and modern manufacturing techniques. To enhance hydraulic efficiency, turbine blades are manufactured with reduced thickness. The combination of thin blades and off-design operation can lead to critical working conditions. An improvement in the design of the turbines is then requested, especially from the structural point of view [10]. A turbine designed for optimal hydraulic performance may not necessarily exhibit optimal structural integrity.

In the last decades, several failures have occurred in HHF turbines with blade cracks as one of the main culprits [11]. Thanks to on-site studies and the research activities conducted at the Waterpower Laboratory, it is now known that the blades of the runner are subject to dynamic loads caused by different hydrodynamic phenomena. In general, the main variations of these loads are caused by the Rotor Stator Interaction (RSI) and vortex shedding [12], [13].

1.3 Objectives

It is then important to understand how the blades of a runner behave, their complete characterization permits to determine their answer to the dynamic pressure field. Information such as natural frequencies, vortex shedding frequency and damping are fundamental for studying the fatigue phenomena and so to be able to predict failures and organize maintenance.

To develop this knowledge in 2016 the HiFrancis project started at the Waterpower laboratory. Since then several experiments and numerical simulations have been conducted on different configurations. The initial phase involved simple geometries: a single hydrofoil in a square-section tube then, in the same cross-section, an array of 3 hydrofoils. At the moment, preparations are underway to perform experiments on a circular cascade (CBC) consisting of 8 radially straight hydrofoils Figure 1.5.

This master thesis aims to numerically characterize the hydrodynamic damping of the foils in the CBC for different mode shapes and Reynolds numbers. The set of data obtained will provide input to the large-scale experiments (scheduled in Spring 2024) providing a more comprehensive understanding of the phenomenon.

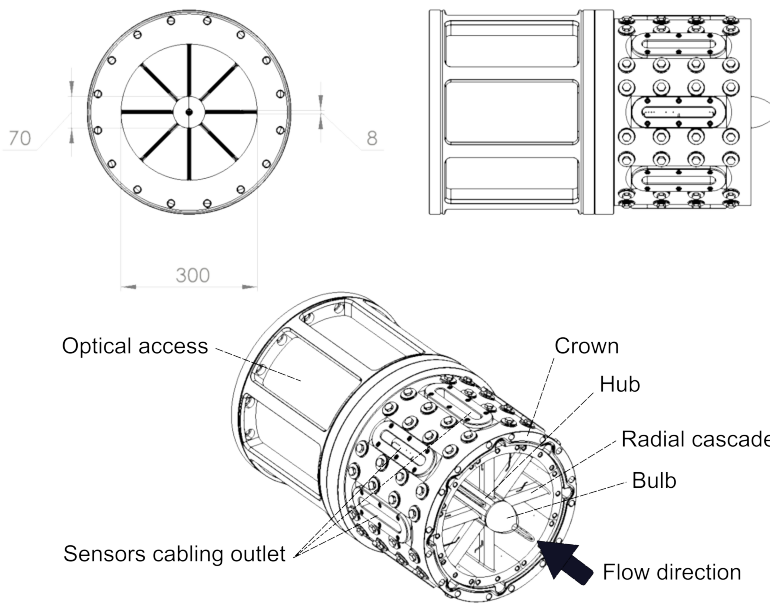


Figure 1.5: Circular Blade Cascade (CBC). Source: Waterpower Laboratory, NTNU

Chapter 2

Literature review

This chapter summarizes previous work on the study of hydrodynamic damping in flowing water. Firstly, literature regarding the theory background is presented, and then, the results of vibration mechanics are discussed. Finally, experimental and numerical approaches regarding similar geometries to the one studied in this master thesis are analysed. Other articles, books and guides have been used to understand linked topics and prepare the numerical simulations but, since they don't refer specifically to hydrodynamic damping, they are not topics for this chapter.

Monette et al. [14] developed the theory for hydrodynamic damping in flowing water based on the momentum exchange between the structure and the flowing fluid. The article proposes also numerical approaches for calculation and provides experimental validation. Their main finding is that the work done by the damping of an under-damped vibrating system can be expressed as a function of the total potential energy U , and the non-dimensional damping ratio ($\zeta = c/c_{cr}$), expressed as the ratio between the system damping and the critical damping values. Assuming a harmonic motion and negligible influence of the water flow on the mode shapes relative to still water, the energy exchanged between the structure and the fluid is equal to the work done by the damping. So, by extracting the values of the total potential energy and the fluid work from specific simulations, it is possible to calculate the hydrodynamic damping. Another important result of this article is that the only non-negligible contribution to the total potential energy U is the kinetic energy associated with the vibration of both the structure and the fluid.

Gaiti et al. [15] carried out both numerical simulations and experiments on the CBC to evaluate the natural frequencies and mode shapes of the structure in still water. The results show that while the first ones are heavily

affected by the presence of the fluid, resulting in a decrease in value compared to the case of air, the mode shapes remain approximately the same.

Pirocca [16] conducted modal and modal acoustic numerical simulations on different CBC geometries to design the one now installed at the Waterpower Laboratory. The experimental values obtained by Gaiti et al. match with the ones expected from Pirocca's work.

Bergan et al. [13] performed experiments and simulations on a submerged, double-fixed hydrofoil. The study considered different layouts, a single hydrofoil and a linear cascade with three hydrofoils in a square cross-section. Two trailing edge geometries were considered, "F0" asymmetric and "F1" symmetric. The results showed a clear trend: above lock-in velocities, a linear dependence was observed, the damping ratio increases with the velocity, while it remains approximately constant under the lock-in velocity. This behaviour, consistent with earlier investigations [17], [18], displayed a discontinuity near the lock-in region, where the natural frequency of the structure matches the vortex shedding one. This happens for both the geometries and for both experiments and simulations and seems related to a phase shift in the vortex shedding. However, uncertainty remains about whether this phenomenon translates to radial cascades or an increased number of hydrofoils. A method to compare results from different geometries was also developed using the modified reduced velocity defined as the ratio between the water velocity and the natural frequency of the foil.

Tengs et al. [19] carried out a one-way coupled FSI simulation on a single submerged, double-fixed hydrofoil in a square test section. Experimental validation of the numerical results has also been performed. In this analysis, a prescribed frequency and amplitude, determined by modal acoustic analysis, were applied to the hydrofoil. The hydrodynamic damping was found to be linearly dependent on flow velocity above the lock-in region, and almost constant before. Additionally, the results showed that, for small deflections, the hydrodynamic damping factor is independent of deflection amplitude. The author suggests further investigation is needed with a configuration more closely resembling a Francis turbine, such as a CBC.

Chapter 3

Theory

The following chapter presents the relevant theory required to understand the physics and the numerical modelling of the phenomenon studied in this master thesis. Firstly, an overview of fluid-structure interaction and related algorithms is introduced, then fluid dynamics phenomena in the turbine are discussed and analyzed. Subsequently, fundamental concepts of Computational Fluid Dynamics (CFD) are shown and finally governing equations for structural mechanics, fatigue and vibration mechanics are reported.

3.1 Fluid structure interaction (FSI)

The interaction between fluids and solids is a common phenomenon in nature, for example, the movement of sand dunes or the deformation of trees caused by wind. These types of interactions are common for all types of fluids, not only air and, in particular circumstances, can be dangerous for both natural and artificial structures. The collapse of the Tacoma-Narrows Bridge in November 1940 is an example of the dramatic consequences that this phenomenon can have (Figure 3.5).

FSI is a multi-physics problem that can only be solved using laws and equations from different physical disciplines; the flow around a body has a strong impact on the structure, and vice versa: the modification of the structure has a non-negligible influence on the flow. The coupling of fluid dynamic and structural dynamic equations describes then the interactions between fluids and structures. Solving such problems it's computationally challenging because of the complex geometries, intricate physics of fluids, and complicated fluid-structure interactions. To reduce the computational effort it is possible to work on how the interaction between fluid and solid is described. Accord-

ing to [20] solution strategies for FSI simulations are divided into monolithic and partitioned methods, and the last one is further divided into two-way and one-way methods.

In a one-way coupling one domain is solved first, the information is then passed to the second one which is solved. This is, for example, the approach adopted in this work: the structural domain is solved using a Finite Element Method (FEM) code, and the results of the simulation, in terms of natural frequencies and mode shapes, are then shared with a CFD simulation where the pressure loads are extracted. A one-way coupling involves no feedback between domains. Figure 3.1.

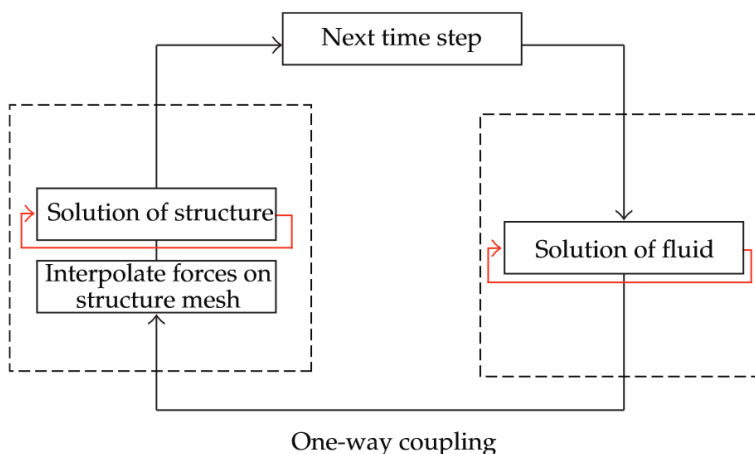


Figure 3.1: Solving algorithm for one-way coupling [20]

The solving method for two-way strong coupling is shown in Figure 3.2, the main difference with a one-way coupling method is the presence of feedback between the fluid and structural domain. For each time step, a converged fluid flow field is required to generate forces acting on the structure. These forces are then interpolated onto the mesh of the structural domain and a converged solution with the applied load is then calculated. The displacements of each mesh node are then evaluated and subsequently interpolated on the fluid mesh. A new converged solution for the deformed fluid domain is calculated and, again, the forces acting on the structure are extracted. This iterative process is carried on such that the changes in the force and displacement are below the set criteria. This iterative implicit process is needed for

each time step of the simulation thus requiring high computational power.

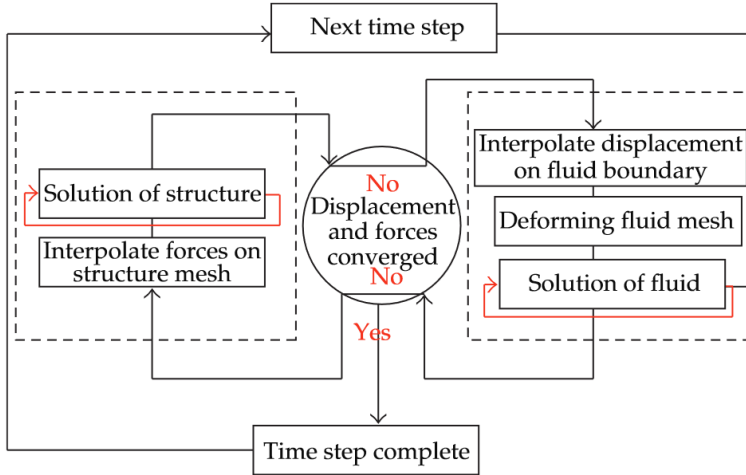


Figure 3.2: Solving algorithm for two-way strong coupling [20]

3.2 Dynamic loads on Francis turbines

As already highlighted in the introduction chapter failures in Francis turbines have, as one of the main culprits, the propagation of cracks caused by fatigue phenomena. It is therefore important to understand and evaluate which are the dynamic loads acting on the runner and the blades during operation.

3.2.1 Pressure pulsations

Rotor stator interaction

According to [12] and [13] approx.80% of the total dynamic stresses of a low specific speed turbine are caused by the Rotor Stator Interaction (RSI). This phenomenon is characterized by pressure fluctuations in the vaneless space, guide vane cascade, the upstream spiral casing and the inlet conduit. The source of the fluctuations is the interaction of two pressure fields:

- rotating pressure field: high and low pressure onboard the runner due to the blade loading, rotating for the stationary domain because it

moves together with the turbine;

- stationary pressure field: high and low pressure around each guide vane.

The rotating pressure field gives fluctuations in the downstream boundary condition of each guide vane passage generating pressure variations. The combination of runner and guide vanes can give constructive interference as Oftebro and Lønning showed in 1966 [21]. Each runner's blade generates a pressure fluctuation each time it passes in front of a guide vane. A pressure pulse occurs every time a runner vane aligns with a guide vane and this happens when the runner has rotated an angle α .

$$\alpha = 2\pi\left(\frac{1}{z_g} - \frac{1}{z_r}\right) \quad (3.1)$$

In Equation 3.1 z_g is the number of guide vanes while z_r is the number of runner blades. So, the temporal distance between the pressure pulse generated by each runner blade corresponds with the time needed to travel the angle α

$$t = \frac{2\pi(z_r - z_g)}{\omega_r z_g z_r} \quad (3.2)$$

where ω_r is the angular velocity of the runner. The produced pressure wave propagates at the speed of $a \pm c$ with a speed of sound in water and c velocity of the water and reaches the next impulse point after a time t_I (D is the diameter of the runner).

$$t_I = \frac{\pi D}{(a \pm c)z_g} \quad (3.3)$$

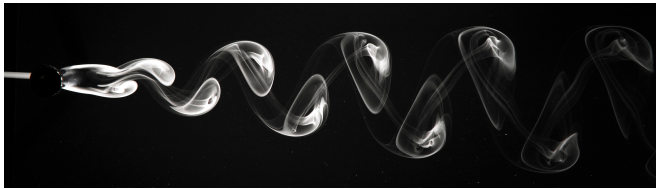
The worst case develops when there is constructive interference and $t = t_I$, a strong pressure oscillation is produced at the frequency f

$$f = \begin{cases} \frac{\omega_r}{2\pi} z_r & \text{if observed in the stationary domain} \\ \frac{\omega_r}{2\pi} z_g & \text{if observed in the rotating domain.} \end{cases} \quad (3.4)$$

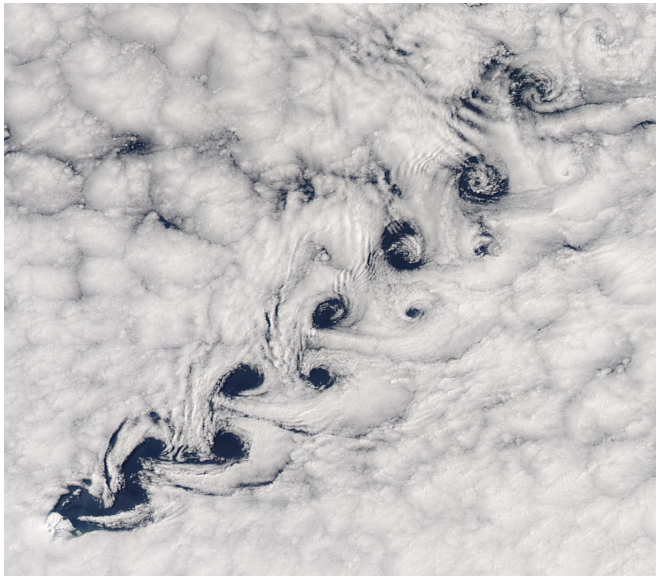
The load frequencies associated with the RSI are then dependent on constructive parameters (number of blades) and the rotating velocity of the turbine. In terms of dynamic loads and so fatigue, the effect of RSI is important. However, since it is not difficult to estimate the frequency of the pressure oscillations, dangerous resonance phenomena can be easily avoided during the operations and even in off-design conditions.

3.2.2 Vortex shedding and Lock-in

Vortex shedding is a fluid dynamic phenomenon that takes place when a fluid flows past a bluff body. Alternated low-pressure eddies generate on the downstream side of the object and detach periodically from either side of the body forming a Kármán vortex street. An oscillating flow takes then place and its characteristics depend on the velocity of the fluid and the size and shape of the body.



(a) Visualisation of the vortex street behind a circular cylinder in air [22]



(b) Vortex shedding as winds pass Heard Island (bottom left) in the southern Indian Ocean resulted in Kármán vortex street in the clouds [23]

Figure 3.3: Vortex shedding on different scales

An important dimensionless parameter for oscillating flows is the Strouhal number, defined as

$$St = \frac{f_s L}{u} \quad (3.5)$$

where f_s is the frequency of the vortex shedding, L is a characteristic length and u is the flow velocity. Strouhal number can be derived with empirical formulas and varies with high Reynolds numbers but, in a large range, it is almost constant [24]. The vortex shedding frequency is then dependent on the flow velocity and so on the Reynolds number.

Not only the frequency but also the amplitude and stability of the phenomenon it is related to the Reynolds number as it is possible to see from Figure 3.4.





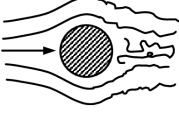

	$Re < 5$	Regime of unseparated flow
	$5 \leq Re < 40$	A fixed pair of vortices in wake
	$40 \leq Re < 90$	Vortex street is laminar
	$90 \leq Re < 150$	Vortex street is laminar
	$150 \leq Re < 300$	Transition range to turbulence in vortex
	$300 \leq Re < 3(10^5)$	Vortex street is fully turbulent
	$3(10^5) \leq Re < 3.5(10^6)$	Laminar boundary layer has undergone turbulent transition and wake is narrower and disorganized
	$3.5(10^6) \leq Re$	Reestablishment of turbulent vortex street

Figure 3.4: Vortex shedding regimes as a function of Re number [25]

The process is then quite stable at low values of the Re number while it becomes more chaotic at higher values, making its study more complex. The working conditions simulated in this master thesis displayed values of Re number from around $7,5 \times 10^5$ to $2,1 \times 10^6$ crossing then the transition regime. Also, the considered geometry is not bluff then the reference value of the Re number can be different.

Alternated low-pressure vortexes are then generated and the invested object will tend to move toward the low-pressure zone starting to vibrate. When the frequency of the vortex shedding is sufficiently close to the natural frequency of the object generating it, lock-in will occur. This is a self-excitation mechanism: the oscillation amplitude of the object will increase affecting the phase of the vortex shedding subsequently the phases of the vortex shedding and the moving object will approach reaching a “locked-in” situation. The amplitude of the oscillation can be considerable and can lead to failures such as the Tacoma Bridge in 1940 Figure 3.5.



Figure 3.5: Tacoma Narrows Bridge collapsing, November 7, 1940 [26]

If the velocity of the fluid, and so the Re number of the flow, are increased above the lock-in region the frequencies of the vortex shedding and the object remain “locked-in” for a certain range.

3.3 Computational fluid dynamics

In the presented work numerical tools have been used to study the flow of the water around the geometry. In CFD software, numerical simulations are employed to analyze systems that involve fluid flow, heat transfer and the associated phenomena such as chemical reactions.

The governing equations of fluid motion represent the conservation laws of physics. The continuity equation describes the conservation of mass while the Navier-Stokes equations the Newton's second law. They are nonlinear partial differential equations and have no analytical solution. A numerical algorithm is hence implemented in CFD software to find a solution by iterative methods. In this work, the adopted software is ANSYS CFX[®] which uses the finite volume method, a special finite difference formulation [27]. The numerical algorithm can be summarized in three main steps:

1. integration of the governing equations of fluid flow over all the (finite) control volumes of the domain;
2. conversion of the resulting integral equations into a system of algebraic equations (discretization);
3. solution of the algebraic equations by an iterative method.

The accuracy of the solution is then strictly related to the finite control volumes, cells part of a numerical grid, named mesh, that represents the fluid domain. A fine mesh, containing a large amount of elements, is more precise than a mesh containing fewer elements but requires more computational power. Also, the shape and the aspect ratio of the cells are important to capture different scale phenomena and, in general, pressure gradients. A trade-off between mesh size and available computational power is always requested, as a rule of thumb an optimal mesh is fine in areas of large gradients while areas of smaller changes have coarser mesh.

3.3.1 Fluid flow governing equations

The fluid flow governing equations represent mathematical statements of the conservation laws of physics:

- mass conservation;
- Newton's second law: change rate of momentum equals the sum of the forces on a fluid particle;

- first law of thermodynamics: change rate of energy equal to the sum of the rate of heat addition to and the rate of work done on a fluid particle;
- equation of state.

They are obtained considering the fluid as a continuum and analysing the flow at macroscopic length scales so that molecular motions can be ignored. Since in the studied system, the energy variation is negligible and the fluid is incompressible (liquid water) the only effective equations are the mass conservation Equation 3.6 and the momentum equations (Newton's second law) Equation 3.7.

$$\operatorname{div}(\vec{u}) = 0 \quad (3.6)$$

$$\rho g_x + \frac{\partial \sigma_{xx}}{\partial x} + \frac{\partial \tau_{yx}}{\partial y} + \frac{\partial \tau_{zx}}{\partial z} = \rho \left(\frac{\partial u}{\partial t} + u \frac{\partial u}{\partial x} + v \frac{\partial u}{\partial y} + w \frac{\partial u}{\partial z} \right) \quad (3.7a)$$

$$\rho g_y + \frac{\partial \tau_{xy}}{\partial x} + \frac{\partial \sigma_{yy}}{\partial y} + \frac{\partial \tau_{zy}}{\partial z} = \rho \left(\frac{\partial v}{\partial t} + u \frac{\partial v}{\partial x} + v \frac{\partial v}{\partial y} + w \frac{\partial v}{\partial z} \right) \quad (3.7b)$$

$$\rho g_z + \frac{\partial \tau_{xz}}{\partial x} + \frac{\partial \tau_{yz}}{\partial y} + \frac{\partial \sigma_{zz}}{\partial z} = \rho \left(\frac{\partial w}{\partial t} + u \frac{\partial w}{\partial x} + v \frac{\partial w}{\partial y} + w \frac{\partial w}{\partial z} \right) \quad (3.7c)$$

In Equation 3.7 t is the time, g_x , g_y and g_z are the components of gravity acceleration along the cartesian coordinate system and u , v and w are the cartesian components of the velocity of the fluid particle \vec{u} . ρ is the fluid density, while σ_{ii} and τ_{ij} are the normal and tangential stresses respectively (the first subscript represents the direction normal to the plane on which the vector acts while the second subscript indicates the vector's direction). For incompressible Newtonian fluids, the stresses are linearly related to the rates of deformation [28] and can be expressed as:

$$\sigma_{xx} = -p + 2\mu \frac{\partial u}{\partial x} \quad (3.8a)$$

$$\sigma_{yy} = -p + 2\mu \frac{\partial v}{\partial y} \quad (3.8b)$$

$$\sigma_{zz} = -p + 2\mu \frac{\partial w}{\partial z} \quad (3.8c)$$

$$\tau_{xy} = \tau_{yx} = \mu \left(\frac{\partial u}{\partial y} + \frac{\partial v}{\partial x} \right) \quad (3.8d)$$

$$\tau_{yz} = \tau_{zy} = \mu \left(\frac{\partial v}{\partial z} + \frac{\partial w}{\partial y} \right) \quad (3.8e)$$

$$\tau_{xy} = \tau_{yx} = \mu \left(\frac{\partial w}{\partial x} + \frac{\partial u}{\partial z} \right) \quad (3.8f)$$

where $p = -\frac{1}{3}(\sigma_{xx} + \sigma_{yy} + \sigma_{zz})$ is the pressure and μ is the dynamic viscosity of the fluid.

Substituting Equation 3.6 and Equation 3.8 in Equation 3.7 and dividing for the density ρ the Navier-Stokes equations (N-S) are obtained [28]:

$$\left(\frac{\partial u}{\partial t} + u \frac{\partial u}{\partial x} + v \frac{\partial u}{\partial y} + w \frac{\partial u}{\partial z} \right) = -\frac{1}{\rho} \frac{\partial p}{\partial x} + \rho g_x + \nu \left(\frac{\partial^2 u}{\partial x^2} + \frac{\partial^2 u}{\partial y^2} + \frac{\partial^2 u}{\partial z^2} \right) \quad (3.9a)$$

$$\left(\frac{\partial v}{\partial t} + u \frac{\partial v}{\partial x} + v \frac{\partial v}{\partial y} + w \frac{\partial v}{\partial z} \right) = -\frac{1}{\rho} \frac{\partial p}{\partial y} + \rho g_y + \nu \left(\frac{\partial^2 v}{\partial x^2} + \frac{\partial^2 v}{\partial y^2} + \frac{\partial^2 v}{\partial z^2} \right) \quad (3.9b)$$

$$\left(\frac{\partial w}{\partial t} + u \frac{\partial w}{\partial x} + v \frac{\partial w}{\partial y} + w \frac{\partial w}{\partial z} \right) = -\frac{1}{\rho} \frac{\partial p}{\partial z} + \rho g_z + \nu \left(\frac{\partial^2 w}{\partial x^2} + \frac{\partial^2 w}{\partial y^2} + \frac{\partial^2 w}{\partial z^2} \right) \quad (3.9c)$$

where $\nu = \frac{\mu}{\rho}$ is the kinematic viscosity.

Reynolds averaged Navier–Stokes equations

The Reynolds number is a dimensionless parameter defined as the ratio between the inertial and viscous forces acting inside the fluid.

$$Re = \frac{\rho u L}{\mu} \quad (3.10)$$

where ρ is the fluid density, u is its velocity, L is a characteristic length and μ is the dynamic viscosity of the fluid. A high value of the Re number ($Re > 4000$) indicates that the flows tend to be dominated by turbulent flow since the inertia forces prevail over the viscous ones. This type of flow is characterized by a chaotic, random behaviour of the fluid parameters, that can be described in terms of their mean values on which superimposed the fluctuations [28]. For the generic fluid propriety ϕ is possible to write:

$$\phi(x_i, t) = \bar{\phi} + \phi'(x_i, t) \quad (3.11)$$

where $\bar{\phi}$ is the mean, or time average, component and ϕ' is the fluctuation.

$$\bar{\phi}(x_i) = \frac{1}{T} \int_{t_0}^{t_0+T} \phi(x_i, t) dt \quad (3.12)$$

In Equation 3.12 the time interval, T , is considerably longer than the period of the longest fluctuations but considerably shorter than any unsteadiness of the average velocity as shown in Figure 3.6.

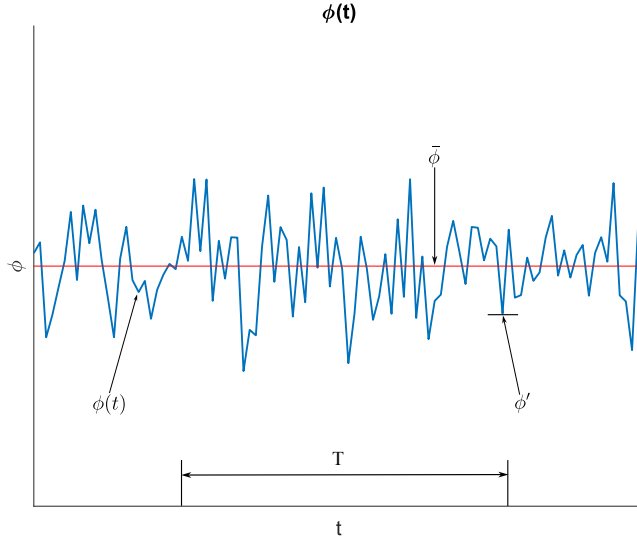


Figure 3.6: Time averaged $\bar{\phi}$ and fluctuating ϕ' description of a generic parameter ϕ for turbulent flow

The pressure, velocity and the velocity components can then be expressed as:

$$p = \bar{p} + p' \quad \vec{u} = \bar{\vec{u}} + \vec{u}' \quad u = \bar{u} + u' \quad v = \bar{v} + v' \quad w = \bar{w} + w' \quad (3.13)$$

substituting Equation 3.13 in Equation 3.9 is it possible to obtain the Reynolds averaged Navier-Stokes equations (RANS) [27]:

$$\begin{aligned} \frac{\partial \bar{u}}{\partial t} + \text{div}(\bar{u}\bar{u}) &= -\frac{1}{\rho} \frac{\partial \bar{p}}{\partial x} + \nu \text{div}(\text{grad}(\bar{u})) + \\ &\frac{1}{\rho} \left[\frac{\partial(-\rho \overline{u'^2})}{\partial x} + \frac{\partial(-\rho \overline{u'v'})}{\partial y} + \frac{\partial(-\rho \overline{u'w'})}{\partial z} \right] \end{aligned} \quad (3.14a)$$

$$\begin{aligned} \frac{\partial \bar{v}}{\partial t} + \text{div}(\bar{v}\bar{u}) &= -\frac{1}{\rho} \frac{\partial \bar{p}}{\partial y} + \nu \text{div}(\text{grad}(\bar{v})) + \\ &\frac{1}{\rho} \left[\frac{\partial(-\overline{\rho u'v'})}{\partial x} + \frac{\partial(-\overline{\rho v'^2})}{\partial y} + \frac{\partial(-\overline{\rho v'w'})}{\partial z} \right] \end{aligned} \quad (3.14b)$$

$$\begin{aligned} \frac{\partial \bar{w}}{\partial t} + \text{div}(\bar{w}\bar{u}) &= -\frac{1}{\rho} \frac{\partial \bar{p}}{\partial z} + \nu \text{div}(\text{grad}(\bar{w})) + \\ &\frac{1}{\rho} \left[\frac{\partial(-\overline{\rho u'w'})}{\partial x} + \frac{\partial(-\overline{\rho v'w'})}{\partial y} + \frac{\partial(-\overline{\rho w'^2})}{\partial z} \right] \end{aligned} \quad (3.14c)$$

The time averaging process introduces a new term in the N-S equations that appears inside the square brackets. The six new terms represent additional turbulent stresses, also called Reynolds stresses. Using the tensor notation they can be written as:

$$\overline{\rho u'_i u'_j}. \quad (3.15)$$

The introduction of Reynolds stresses in RANS equations implies that the equation set is not closed, there are more variables than equations. To close the equations set is then necessary to adopt a turbulence model.

3.3.2 Turbulence modelling

CFD software use an iterative process to solve the N-S equations. In Direct Numerical Simulations (DNS) the Navier–Stokes equations are numerically solved without any turbulence model while the other two main solution methods: Large Eddy Simulations (LES) and RANS require a model for the turbulence. For most engineering purposes it is unnecessary to resolve the details of the turbulent fluctuations. DNS and LES are then not so diffused outside of the research field due to their high cost in terms of computing resources.

In general applications RANS model is adopted due to its good trade-off between flow accuracy and computational needs [27]. As seen in subsection 3.2.1 the adoption of this solution method requires a model for the turbulence to close the equation set. The most used and validated RANS turbulence models are $k - \omega$, $k - \epsilon$ and $k - \omega$ *SST*. They introduce two additional transport equations that allow to close and then solve the RANS equations. In the $k - \omega$ model, proposed by Wilcox, the turbulent kinetic energy k is used as the first variable while the turbulence frequency $\omega = \epsilon/k$ is the second one. This model gets good performances in adverse pressure

gradient boundary layer while it appears highly sensitive to turbulent properties in the free stream. The $k-\epsilon$ model uses the rate of viscous dissipation ϵ instead of the turbulence frequency ω as the second variable. The main limitation of this model is the unsatisfactory near-wall performance for boundary layers with adverse pressure gradients while good results in the free stream are displayed. To exploit the advantages of both methods the $k-\omega$ *SST* turbulence model has been developed as a combination of the $k-\epsilon$ and $k-\omega$ models, it uses a transformation of the $k-\epsilon$ into a $k-\omega$ in the near-wall region and the standard $k-\epsilon$ in the fully turbulent region far from the wall. The simulations performed in this master thesis used the $k-\omega$ *SST* turbulence model, for a detailed breakdown of the theory and equations of the presented models, the reader is recommended to look in [27].

3.4 Structural mechanics

When a load is applied to a structure it induces stresses inside the material that composes it. These stresses can lead to failure in two different ways: static or fatigue. A static failure occurs when static loads exceed the yield strength of the material, this situation does not happen if the structure is well designed and operated, while fatigue failure manifests itself when repeated cyclic loads are applied. The magnitude of the cyclic stress is normally low, less than the yield stress of the material and is rather the number of cycles that brings the structure to failure [29]. The dynamic loads presented in section 3.2 create cyclic stresses in the runner material and so fatigue failures are the most common and dangerous ones [13].

3.4.1 Fatigue

The fatigue characterization of a material is represented by the stress vs number of cycles (S-N) curve. It shows the number of cycles that the material can withstand at a specific stress level. Depending on the geometry, surface finishing and other parameters, the value changes and needs to be adjusted for the specific application with appropriate factors. Each load cycle introduces damage in the material that is added to the one already present, the accumulated damage can be estimated by e.g., the Miner-Palmgren rule [30]:

$$\sum_{i=1}^k \frac{n_i}{N_i} = D \quad (3.16)$$

where n_i is the number of stress cycles at load i , and N_i is the number of stress cycles to failure at load i . When $D = 1$ the material is assumed to be at the end of its lifetime. Fatigue failure is characterized by sudden plastic deformation that leads to a break preceded by a fracture inception and propagation phase.

To obtain the N-S curve of a material experiments are conducted on test samples: they are subjected to repeated cycles of measurable stress and the number of cycles N before failure is plotted against the corresponding stress amplitude S . Two main behaviours can be observed: for ferrous and titanium alloys the curve will become horizontal, after high values of N , while, for other materials, it continues to decrease. For ferrous material is then possible to evaluate a fatigue limit, if a stress with amplitude equal to or lower than the fatigue limit is applied the material will not fail for any cycle number. For nonferrous materials, that don't display any horizontal asymptote, the fatigue limit cannot be defined. A fatigue strength or a fatigue life can be evaluated: fatigue strength is the permissible stress amplitude that can be applied to the material to last for a prescribed number of cycles while fatigue life is the number of cycles the material can withstand before failing at a prescribed stress amplitude.

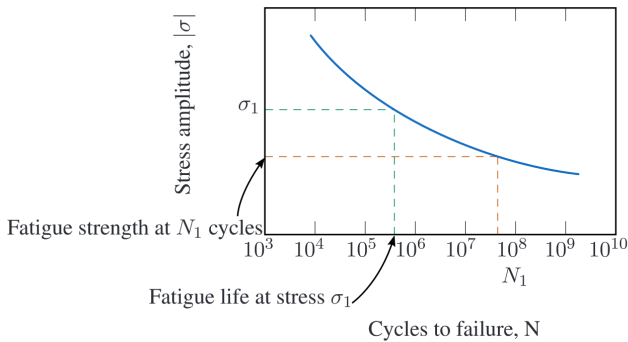


Figure 3.7: S-N curve for a nonferrous alloy [13]

Fatigue phenomena are then strictly related to cycle number and stresses; in a Francis turbine, the first ones are linked with the frequencies of RSI, RVR and vortex shedding while the second ones depend on the loads. Knowing these parameters it is possible to fully design the turbine and its maintenance. While it is relatively easy to evaluate the loads on the runner during nominal working conditions the same is not true during resonance phenom-

ena. For this specific situation, stress values can be determined starting from displacement information ($\varepsilon \leftrightarrow \sigma$ through the Young module) that can be obtained from measurements on the machine or, during the design phase, from simulations. In both cases the value of the displacement is strongly dependent on the damping as will be shown in subsection 3.4.3, it is then important to evaluate it, also to be sure to avoid auto-excitation phenomena.

3.4.2 Finite element method

Continuous problems are usually described by differential equations that can only be solved exactly by mathematical manipulation. The available mathematical techniques limit then the solution possibilities to oversimplified situations [31]. To overcome this problem several discretization methods have been proposed, they all involve an approximation but the greater the number of discrete variables the smaller the approximation.

Finite Element Method (FEM) is a widely used numerical method for solving differential equations: the system is divided into a finite number of parts the behaviour of which is specified by a finite number of parameters [31]. Elements are connected through nodes forming a mesh and the global set of equations from the FEM procedure is solved using a direct solver or an iterative one. The solution of the complete system is an assembly of the element's solution. In this thesis, the commercial FEM software ANSYS Mechanical[®] is used.

3.4.3 Vibrations in multiple degrees of freedom systems (MDOF)

The dynamic analysis of most of the real structure cannot be described adequately by a single-degree-of-freedom system (SDOF), a system with multiple degrees of freedom is needed. The general motion's equation of a linear system with N degree of freedom is:

$$\mathbf{M}\ddot{\vec{u}} + \mathbf{C}\dot{\vec{u}} + \mathbf{K}\vec{u} = \vec{l}(t) \quad (3.17)$$

where $\vec{u}(t)$ is the displacement vector (physical or generalized) and $\vec{l}(t)$ is the corresponding load vector, both of them have $N \times 1$ dimension. Each superscript dot represents a temporal derivative. \mathbf{M} , \mathbf{C} and \mathbf{K} are respectively the mass, the viscous damping and the stiffness matrix of the system and are all $N \times N$.

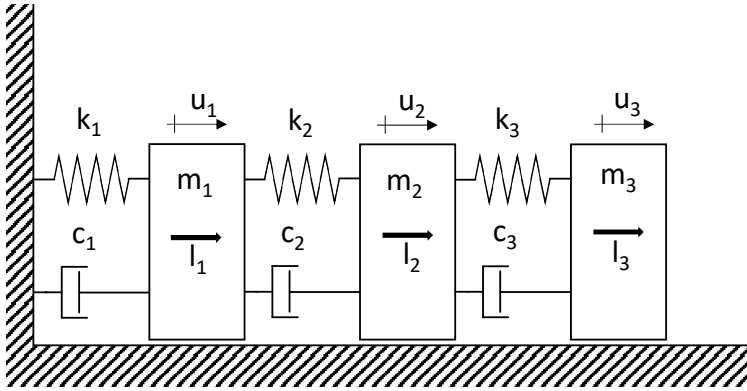


Figure 3.8: MDOF system

If the system moves with harmonic motion the displacement vector can be written using the complex notation:

$$\vec{u} = \vec{u}_0 e^{st} \quad (3.18)$$

with s being a complex number. Substituting Equation 3.18 in Equation 3.17 is it possible to write:

$$(s^2 \mathbf{M} + s \mathbf{C} + \mathbf{K}) \vec{u}_0 = \vec{l}_0 e^{i\phi} \quad (3.19)$$

where \vec{u}_0 and \vec{l}_0 are generally complex and ϕ is the phase shift between load and deflection. For each DOF, if no external forces are applied to the system, Equation 3.20 can be solved for s obtaining:

$$s = -\omega_n \zeta \pm i \omega_n \sqrt{1 - \zeta^2} \quad (3.20)$$

where $\omega_n^2 = K/M$ is the natural frequency, $\zeta = C/(2M\omega_n)$ is the damping ratio and C is the actual damping present in the system. The product $2M\omega_n$ is called critical damping, if a system is critically damped ($\zeta = 1$) it returns asymptotically to a stable equilibrium position without any vibration. According to the value of damping ratio ζ the response of the system to a transitory perturbation is different:

- $\zeta = 0$ undamped vibration, the response is pure harmonic;
- $\zeta > 1$ overdamped vibration;

- $0 < \zeta < 1$ underdamped vibration.

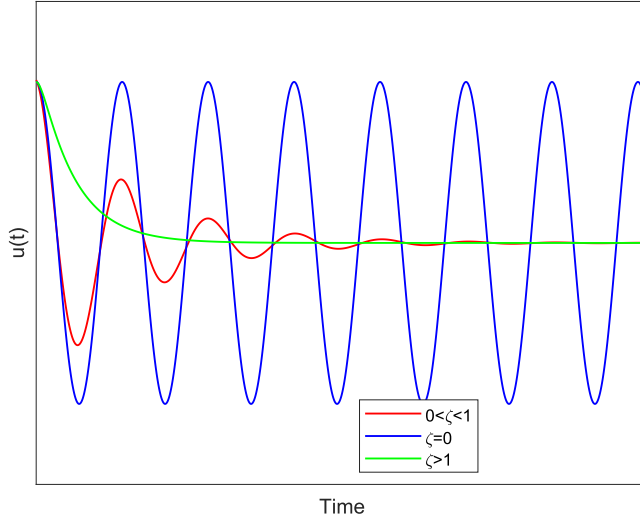


Figure 3.9: Response of a free damped system to a step input as a function of the damping ratio

When the damped system is subjected to a harmonic forcing the regime response for every degree of freedom can be expressed with the transfer function:

$$u(t) = \frac{l_0}{k} \frac{1}{\sqrt{(1 - (\frac{\omega}{\omega_n})^2)^2 + (2\zeta(\frac{\omega}{\omega_n})^2)^2}} \cos(\omega t + \arctan \frac{-2\zeta \frac{\omega}{\omega_n}}{1 - (\frac{\omega}{\omega_n})^2}) \quad (3.21)$$

where l_0 represents the forcing magnitude, k is the stiffness, ζ the damping ratio, ω_n the natural frequency of the system while ω is the forcing frequency. Compactly is possible to write:

$$u(t) = \frac{l_0}{k} |H(w)| \cos \left(\omega t + \arctan \frac{-2\zeta \frac{\omega}{\omega_n}}{1 - (\frac{\omega}{\omega_n})^2} \right) \quad (3.22)$$

Plotting the magnitude of the transfer function as a function of the ratio $\frac{\omega}{\omega_n}$ makes the resonance phenomenon clear and also highlights the influence of the damping on the vibration motion's amplitude.

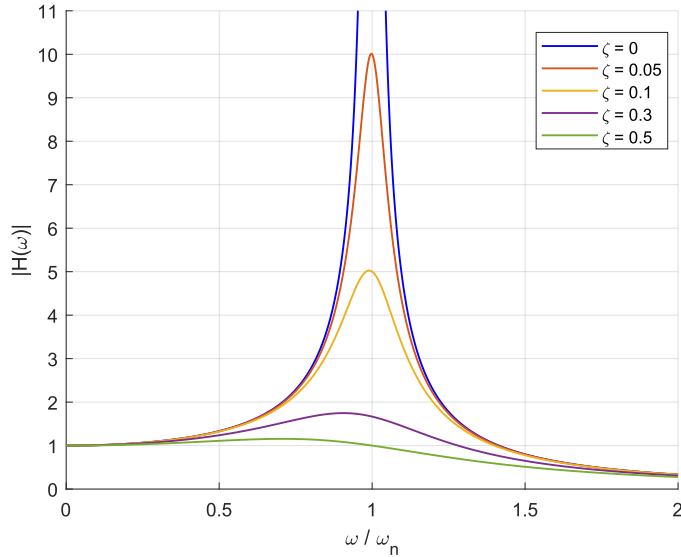


Figure 3.10: Transfer function amplitude depending on different values of damping ratio ζ

When the frequency of the forcing function is equal or close to the natural frequency of the system ($\omega/\omega_n = 1$), the amplitude of the forced vibration becomes very large (e.g. with $\zeta = 0.05$, the amplitude is ten times the static one (l_0/k)). In the case of zero damping, the amplitude tends to infinity. The fact that for small damping values, in resonance conditions, the amplitude can reach very high values is of practical engineering interest, as vibrations of significant amplitude can pose a danger to the integrity of the system.

Cyclic symmetry

The way a structure vibrates depends on its geometry, constraints, applied loads and frequencies. During the vibrating motion stationary regions are observable. They are called nodes and are particularly relevant for resonance phenomena. During resonance, the natural frequency of the structure matches the existing one and the loads are not applied on the nodes since, in that case, the work done on the structure would be null.

For disc-like structures such as runners the node concept can be generalized to Nodal Diameters (ND), regions of the structure where the mode shapes

contain lines of zero displacement. When the object presents a cyclic symmetry, i.e. a portion of it, characterized by a divisor integer angle is repeated a finite number of times around the axis of symmetry to obtain the full geometry, specific vibrating behaviours can be observed. The different parts of the structure can move together or in phase opposition, different phase angles are also possible: these mode shapes usually appear as travelling waves and are the ones that differentiate the behaviour of a linear structure from one with a rotational symmetry.

3.4.4 Damping

Damping is a phenomenon present in all oscillatory real systems and its primary effect is to dissipate energy in the form of heat or sound. The energy loss due to the damping causes a decay of the amplitude of free vibration or, in a forced-vibration system at a steady state, the need for energy supply by the exaction to maintain the motion.

Many different mechanisms can cause damping in a system:

- material internal friction: material damping;
- friction between parts which compose the system: Coulomb and structural damping;
- presence of viscous dampers: viscous damping;
- interaction between a fluid and the system: aero/hydrodynamic damping.

Material damping, also known as hysteretic damping, can be seen as an internal frictional loss due to molecular motion that dissipates energy as heat. The material deformation causes energy loss that is represented by the area enclosed in the hysteresis graph Figure 3.11.

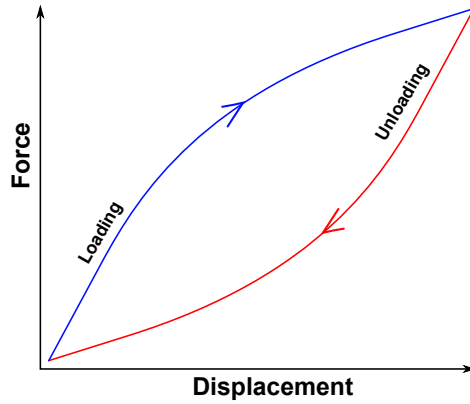


Figure 3.11: Hysteresis graph for a generic metallic material [32]

This type of damping is typically independent of the excitation frequency, except for viscoelastic material such as rubber, but proportional to the displacement.

Coulomb frictional damping arises from the energy lost in the sliding of part in contact, the energy of the system decreases due to frictional losses and it is dissipated into heat and noise. If the parts in contact are connected through mechanical junctions (screwing, rivetting, etc.) their relative movement will be minimum but, if present, will introduce a specific frictional damping called structural damping.

Most of the mechanical systems are equipped with specific tools called dampers to manage vibrations. The most common type is the viscous one, in this case, the exerted damping force is proportional to the movement velocity $F = c \cdot u$. The dissipated energy is proportional to the excitation frequency and the square of the displacement.

If the structure vibrates inside a fluid a new damping component is present. The interaction between the fluid and the system influences its motion absorbing energy. In specific situations, the fluid can provide energy to the structure leading to dangerous auto-excitation phenomena. If the fluid is air its effect is usually negligible while it becomes more important for heavier fluids, like water. In this specific case, the term hydrodynamic damping is used.

For complex mechanical systems, where different types of damping act, can be useful to unite them together: equivalent viscous damping and Raleigh damping models are frequently employed [29].

3.4.5 Modal and modal acoustic analysis

Modal and modal acoustic analysis are fundamental for the study of mechanical vibrations. They allow to calculate the natural frequencies and mode shapes of the structure vibrating respectively in air (or vacuum) or inside a fluid (such as water). In this master thesis, both analyses have been numerically performed imposing the material damping equal to zero.

Modal analysis

With the hypotheses explicated above the CBC can be modelled as an unloaded and undamped structure with constant stiffness and mass. The motion equation is then:

$$\mathbf{M}\ddot{\vec{u}} + \mathbf{K}\vec{u} = \vec{0} \quad (3.23)$$

and considering the system linear, the free vibration response will be harmonic.

$$\vec{u} = \vec{\varphi}_j \cos \omega_j t \quad (3.24)$$

$\vec{\varphi}_j$ is the eigenvector that represents the deformed shape of the structure when vibrating at the j^{th} natural frequency ω_j . Substituting Equation 3.24 in Equation 3.23 the following expression is obtained.

$$(\mathbf{K} - \omega_j^2 \mathbf{M})\vec{\varphi}_j = \vec{0} \quad (3.25)$$

Looking for a non-trivial solution the eigenproblem formula needs to be solved:

$$|\mathbf{K} - \omega^2 \mathbf{M}| = 0 \quad (3.26)$$

resulting in n eigenvalues ω^2 that subsisted in Equation 3.25 gives the n $\vec{\varphi}_j$ eigenvectors. Each eigenvector has many components as the number of DOF of the system and represents the shape of the deformation at the

frequency ω_j but not the amplitude value, which is usually normalized to one. The values of the natural frequencies of the system are then obtained from Equation 3.27.

$$f_j = \frac{\omega_j}{2\pi} \quad (3.27)$$

Modal acoustic analysis

The CBC vibrates inside flowing water which presence influences the motion of the structure. To keep into account the water effect a modal acoustic analysis is needed.

Acoustic analysis simulates the generation and propagation properties of the acoustic waves in the given environment: the structure, as well as the fluid medium, is modelled and natural frequencies and mode shapes are extracted. ANSYS Mechanical[®] enables to modelling of pure acoustic problems and fluid-structure interaction (FSI) problems, in this work, a coupled simulation has been carried out. A coupled acoustic-structural interaction analysis solves the structural dynamics equation, the linearized Navier-Stokes equations of fluid momentum, and the flow continuity equation together. The resulting finite element dynamic matrix equation is [33]:

$$\begin{aligned} \begin{Bmatrix} \{l_S\} \\ \{l_F\} \end{Bmatrix} &= \begin{bmatrix} [\mathbf{M}_S] & 0 \\ \rho_0 [\mathbf{R}]^T & [\mathbf{M}_F] \end{bmatrix} \begin{Bmatrix} \{\ddot{u}_e\} \\ \{\ddot{p}_e\} \end{Bmatrix} + \begin{bmatrix} [\mathbf{C}_S] & 0 \\ 0 & [\mathbf{C}_F] \end{bmatrix} \begin{Bmatrix} \{\dot{u}_e\} \\ \{\dot{p}_e\} \end{Bmatrix} \\ &+ \begin{bmatrix} [\mathbf{K}_S] & -[\mathbf{R}] \\ 0 & [\mathbf{K}_F] \end{bmatrix} \begin{Bmatrix} \{u_e\} \\ \{p_e\} \end{Bmatrix} \end{aligned} \quad (3.28)$$

where \mathbf{M}_i , \mathbf{C}_i , \mathbf{K}_i are the mass, damping and stiffness matrix respectively, of the structure if $i = S$, of the fluid if $i = F$. The same nomenclature is used for the external force vector \vec{l}_i while \vec{u}_e is the displacement vector and \vec{p}_e is the pressure one. ρ_0 is, instead, the density of the acoustic fluid and \mathbf{R} is the matrix that represents the coupling conditions on the interface between the acoustic fluid and the structure. Equation 3.28 solves for acoustic pressure propagation in the acoustic domain and structural deformation, considering the interaction between the acoustic and structural domain such as the added mass effect.

When a submerged body vibrates the surrounding fluid must be displaced and so accelerated. Inertia and fluid forces are then involved in opposing the motion of the object. Their effect can be modelled as an additional mass that

moves together with the structure which therefore is called “added mass” [34]. Considering a simple spring-mass system (stiffness K , mass M), with one DOF, its natural frequency in vacuum (or air) is given by:

$$f_n = \sqrt{\frac{K}{M}} \quad (3.29)$$

if the same system is submerged in a fluid its natural frequency is:

$$f_{n,fluid} = \sqrt{\frac{K}{M + M'}} \quad (3.30)$$

where M' is the added mass. The same consideration can be extended to more complex systems such as the CBC which will then display lower natural frequencies. Specific research carried out at the Waterpower Laboratory (NTNU) by Gaiti et al. showed that, unlike the natural frequencies, the mode shapes of the CBC in air and in water are quite similar [15].

Methodology

This chapter presents the path followed to obtain the hydrodynamic damping of hydrofoils arranged in the CBC. Firstly an introduction to needed parameters and relations is given, and then a summary of the simulations is provided.

4.1 Hydrodynamic damping

The foundation of the work conducted in this master thesis is the article of C. Monette et al. [14] where the theory of hydrodynamic damping in flowing water is developed. As previously mentioned the goal is the characterization of the hydrodynamic damping, we are then interested in evaluating the damping ratio ζ for different mode shapes and flow velocities.

Monette et al. obtained the following relation for the work done by the damping of an under-damped vibrating system W_D :

$$W_D = 4\pi\zeta U \quad (4.1)$$

where $\zeta = c/c_{cr}$ is the damping ratio and U is the total potential energy of the system including both fluid and structure. According to literature [35] and [36] is possible to state that the damping force F_D is proportional to the flow velocity and that the stiffness force F_K acting in the structure is negligible ($F_K \rightarrow 0$). Under these assumptions, the total potential energy of the system U is given from the sum of the kinetic energies of the structure and the fluid vibrating at the natural frequency of the structure in the fluid.

$$U = \frac{1}{2}(d_s\rho_s + d_w\rho_w)\Omega^2 \iint u_0^2(x, y) dx dy \quad (4.2)$$

In Equation 4.2 $d_s \rho_s$ and $d_w \rho_w$ are respectively the mass per unit area of the structure and the fluid, Ω is the natural frequency of the structure in the fluid and u_0 is the displacement amplitude. The reference system used in Equation 4.2 is the one reported in Figure 4.1, the velocity component accounted in U is then only the one in the same direction as the deformation.

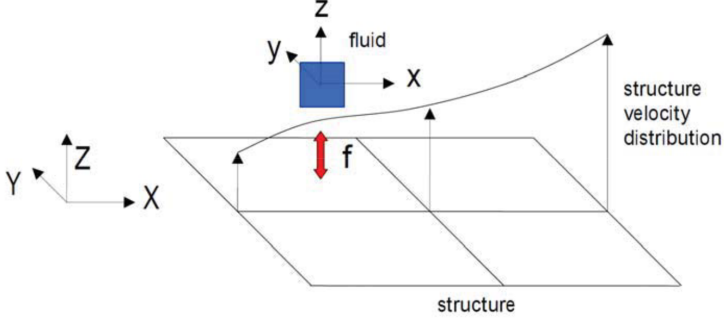


Figure 4.1: Fluid particle moving on a vibrating structure [14]

The article proposes a CFD approach to the problem that exploits the possibility of CFD codes to handle defined mesh motion during transient calculations. Assuming that the differences between the mode shapes in flowing water and the ones in still water are negligible, the damping work W_D can be extracted from a transient CFD simulation as the work done by the fluid forces on the structure per cycle.

$$W_D = \int_{t_0}^{t_0+T} \int_A p \vec{v} \cdot \hat{n} dA dt \quad (4.3)$$

In Equation 4.3 t_0 is the starting time of the vibration cycle while T is its period. A is the surface of the hydrofoil, p is the pressure, \vec{v} is the velocity of deformation of the blade while \hat{n} the normal direction exiting the blade. In ANSYS CFX[®] this integral can be calculated using the command “aerodynamic damping” available in the output controls. A positive value of W_D indicates that the hydrofoil dissipates energy in the fluid while a negative value shows a resonance situation.

The value of the total potential energy U , equal to the sum of the kinetic energy of the structure and the fluid, can instead be obtained through a “user-defined result” in a modal acoustic simulation in ANSYS Mechanical[®].

It is then possible to evaluate the hydrodynamic damping for any combination of nodal diameter and velocity by simply solving for ζ Equation 4.1 so:

$$\zeta = \frac{W_D}{4\pi U} \quad (4.4)$$

In the following chapters and sections, we will refer to the denominator of Equation 4.4 as the “normalization factor”.

Damping work (W_D)

Initially, the approach was to use a direct one-way FSI to extract the damping work made by the water on the foil. A first trial was done by performing some pure CFD simulations to obtain the pressure field around the hydrofoil. Importing the results as external load in a structural simulation the displacement field could have been evaluated and then, after further calculations, the value of the hydrodynamic damping.

Since the first attempts was clear that this procedure was not suitable. Previous experiments conducted at the Waterpower Laboratory showed, for the considered geometry, the presence of the vortex shedding that was not visible in the simulations. The numerical model did not faithfully represent reality due mainly to two reasons: mesh and turbulence modelling. The mesh was prepared with Turbogrid[®], its quality was good but the number of elements, even if quite high (≈ 2.5 million), was not enough to catch the occurring phenomena. The chosen turbulence model was, at first, the $k - \omega$ *SST* and was not able to correctly evaluate the flow motion.

Understood and settled these errors the new stumbling block was the computational time. The employed *SAS* model is more computationally expensive than $k - \omega$ *SST* and the increased number of elements (≈ 12 million) leads to a too high computational request. To get an idea, a very similar simulation was performed by a colleague using Aura, a High-Performance Computer (HPC) available at the Waterpower Laboratory and took around 10 days. A so long computational time was unacceptable for the research carried on in this master thesis since several of these simulations were needed.

A reverse one-way FSI simulation, called in Ansys[®] user guide “Flutter simulation”, was then used. The structural domain was solved first and the results were imported in a CFD simulation. Mode shapes and natural frequency of the CBC in still water were evaluated from a modal acoustic analysis on Ansys Mechanical[®]. Exploiting then the possibility of imposing a periodic displacement to the mesh in Ansys CFX[®] the hydrofoil was made vibrate in a CFD transient simulation. The value of W_D was then extracted

using the available command “aerodynamic damping”.

This approach still requires a remarkable quantity of time but was manageable. Since the correct displacement field is imposed a coarser mesh and a simpler turbulence model could be used. In the previous case, an error in the solving of the fluid domain would have led to imprecise values of pressure and displacement while, using a “reverse one-way” approach, only the pressure field could present any inaccuracy.

4.2 Modal acoustic simulation on Ansys Mechanical[®]

This simulation is the first that needs to be solved. The 3D model of one hydrofoil and the surrounding fluid was prepared and meshed. It was possible to model only 1/8 of the CBC since the command “cyclic symmetry” has been used (Figure 4.2).

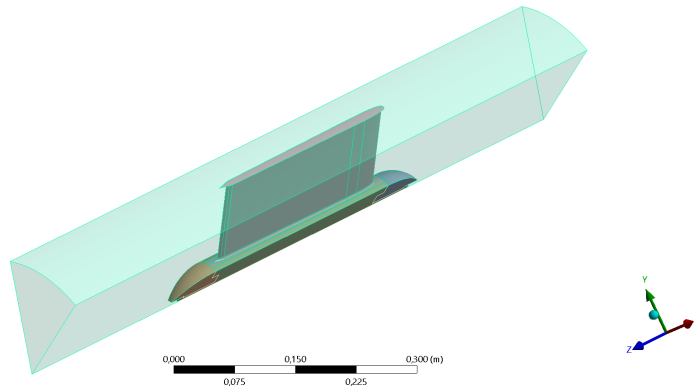


Figure 4.2: Modelled system for the modal acoustic analysis

Elements “SOLID187” and “FLUID221” were adopted respectively for the structure and the fluid Figure 4.3.

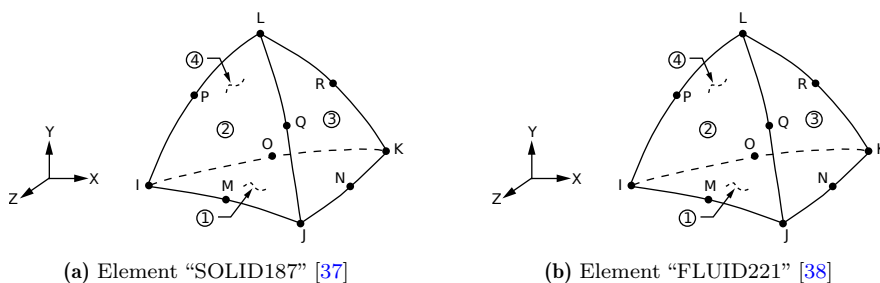


Figure 4.3: Elements of the mesh adopted in the modal acoustic simulation. Each of them has 10 nodes with 3 DOF

Using an APDL command the natural frequency of the structure and its eigenvectors were extracted as csv file while the kinetic energy was evaluated through a specific “user-defined result” available in the post-processing.

4.3 Reverse one-way simulation on Ansys CFX[®]

This type of simulation, improperly defined by Ansys user guides[®] as “Flutter simulations” can be summarized in four main phases:

1. geometry preparation;
2. meshing;
3. initialization with a steady state simulation;
4. transient simulation.

The geometry used in the simulation is the same adopted for the modal acoustic analysis and the mesh was created using Ansys Turbogrid[®], a specific software dedicated to meshing in turbomachinery. The mesh was optimized to obtain good values of y^+ for each testing velocity, the value of Re number was then requested by the software. A steady state simulation was then run as initialization of the transient one, modelling two passages, as shown in Figure 4.4.

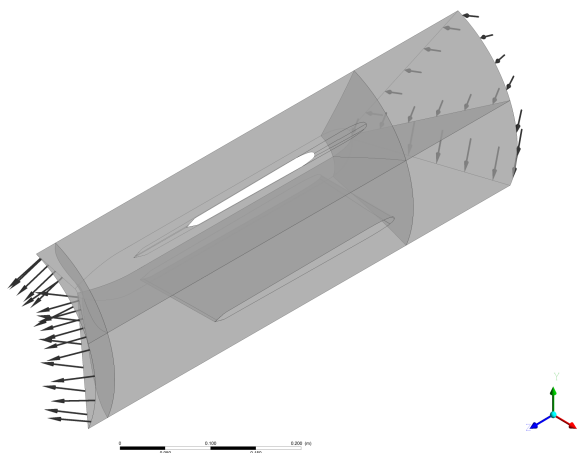


Figure 4.4: Set up configuration for both steady and transient simulations. Two blades and two passages are modelled

The used boundary conditions are mass flow rate at the inlet, calculated to obtain a specific velocity at the foil leading edge, and a relative pressure at the outlet equal to zero.

Subsequently, a transient simulation was run with the same set-up, where a periodic mesh displacement, equal to the mode shape of the hydrofoil, was imposed on its surface. The maximum amplitude was settled to 0,05mm. Only two passages were simulated on Ansys CFX[®] to reduce the computational time. This was possible since the Fourier Transformation method was employed in the transient simulation. The periodic quantities were measured on a specified sampling plane and then suitably reported on the defined periodic surfaces. Exploiting this procedure has been possible to perform the calculations on any nodal diameter modelling only two fluid passages. In the post-processing, the values of y^+ , Courant number and flow velocity at the leading edge were checked at different time steps and, through the “aerodynamic damping” command available in the output control, the value of the fluid work on each blade was extracted.

Results and discussions

The present chapter presents and discusses the results of the performed simulations. The available computational power, even if rather high, was the bottleneck of the work that has to be therefore focused only on the first mode shape of nodal diameter zero and one, indicated respectively as ND0₁ and ND1₁. A point for the nodal diameter 4, mode 1 (ND4₁) has also been evaluated to check the accuracy. From now on, for better ease of reading the work, the subscript 1 after the nodal diameter that indicates the first mode shape, will be neglected.

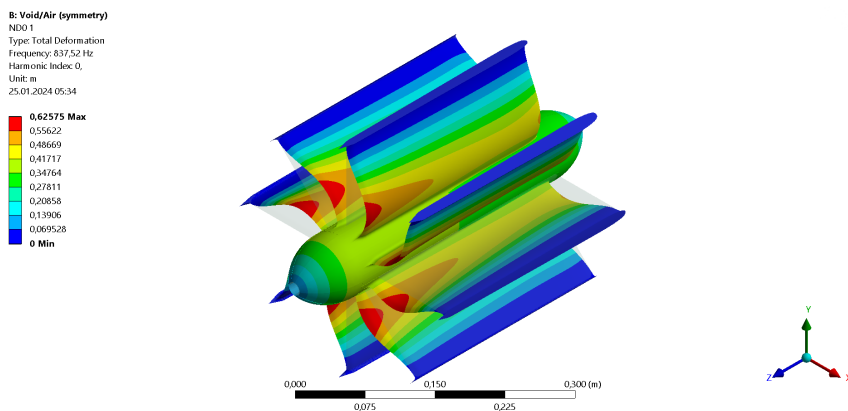
5.1 Natural frequencies, mode shapes and kinetic energy

From the modal acoustic simulation performed on Ansys Mechanical[®] the natural frequencies and mode shapes of the CBC have been extracted. They show a good agreement with the values and shapes found by Gaiti et. al. in [15], natural frequencies are lower than the ones in the air due to the effect of the added mass, while the mode shapes are mostly the same.

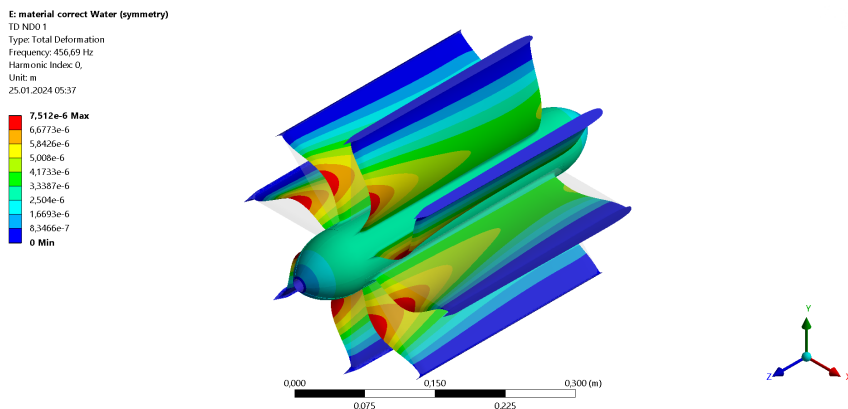
Table 5.1: Natural frequencies of the first mode shape of each nodal diameter

Nodal Diameter	Frequency [Hz]
ND0	456.7
ND1	553.6
ND2	451.5
ND3	394.6
ND4	377.6

In Figure 5.1 and Figure 5.2 a comparison between the mode shapes of the CBC in air and water is shown. It can be observed that the way in which the structure deforms is the same for both mediums. As already exposed in subsection 3.4.5 the deformation values are arbitrary and should not be considered.



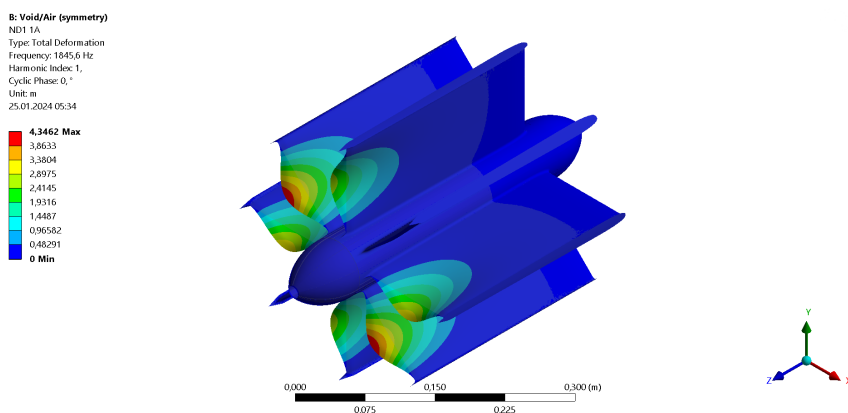
(a) Nodal diameter 0, mode shape 1 in air



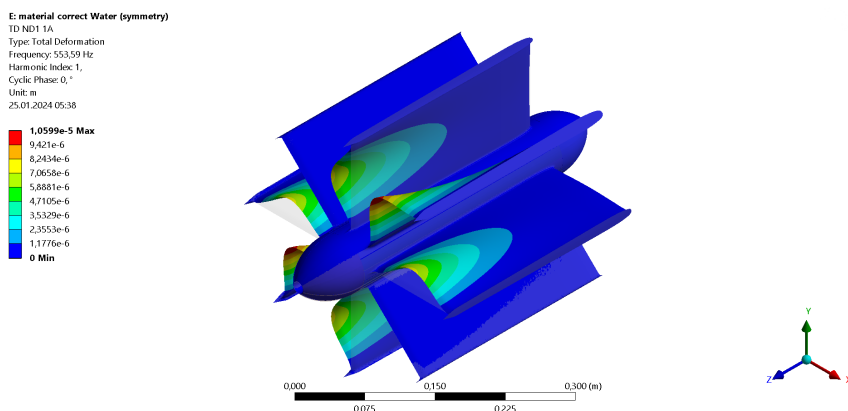
(b) Nodal diameter 0, mode shape 1 in water

Figure 5.1: Comparison between the first mode shape of nodal diameter 0 in air (a) and water (b)

5.1. Natural frequencies, mode shapes and kinetic energy



(a) Nodal diameter 1, mode shape 1 in air



(b) Nodal diameter 1, mode shape 1 in water

Figure 5.2: Comparison between the first mode shape of nodal diameter 1 in air (a) and water (b)

Finally, it is possible to note a different trend between ND0 and ND1. The former exhibits a more uniform deformation across the entire foil when in the air rather than in water, while the latter shows the opposite behaviour.

From the same simulation the values of the kinetic energy Equation 4.2 have been extracted adopting a user-defined command, they are reported in Table 5.2. The results are related to a maximum displacement value that is different for each mode shape and calculated by the modal acoustic analysis.

Table 5.2: Kinetic energy values and refereed maximum displacement for the first mode shape of each nodal diameter

Nodal Diameter	Kinetic energy [JE-04]	Max displacement [mE-06]
ND0	5.9749	7.5120
ND1	2.3159	1.0599E+01
ND2	2.2096	8.7747
ND3	2.5408	7.8521
ND4	2.5408	5.3818

In the performed CFD simulations, the maximum displacement has been imposed equal to 0.05mm. According to Tengs et al. [19] that value can be chosen freely as long as small (less than 0,5mm) since the hydrodynamic damping is independent of the displacement. The results presented in Table 5.2 cannot be used directly, they need to be normalized and then related to the imposed displacement, the result of this procedure is reported in Table 5.3.

Table 5.3: Kinetic energy values refereed to a maximum displacement of 0.05mm for each nodal diameter

Nodal Diameter	Kinetic energy [JE-02]
ND0	2.6470
ND1	5.1538E-01
ND2	7.1745E-01
ND3	1.0302
ND4	2.1931

5.2 Work of the blade on the fluid W_D

The W_D values were derived from the CFD simulations discussed in section 4.3 and are reported in Table 5.4. The ‘‘Aerodynamic damping’’ command, accessible in the ‘‘Output control’’ was employed with a normalization factor set to one. Two different integration periods, namely full and moving, were applied to calculate the integral Equation 4.3 on each of the two hydrofoils in the model. Hydrodynamic damping was then computed for both hydrofoils using two distinct integration methods, and after achieving convergence, the four values converged to alignment. Each provided data point represents the average of the four W_D values, each of them calculated

as the mean of the last 25 measurements at convergence.

Table 5.4: Work values W_D for each combination of nodal diameter and velocity

Velocity [m/s]	W_D [JE-03]	
	ND0	ND1
0.5	1.5429	—
1	1.5316	—
2	1.6474	—
3	1.6673	—
4	1.5947	1.7937
5	1.5401	—
6	1.4983	—
7	1.4465	—
8	1.4218	1.6038
9	1.3988	1.5763
10	1.4278	—
12	1.5167	1.7224
14	1.9590	1.8705

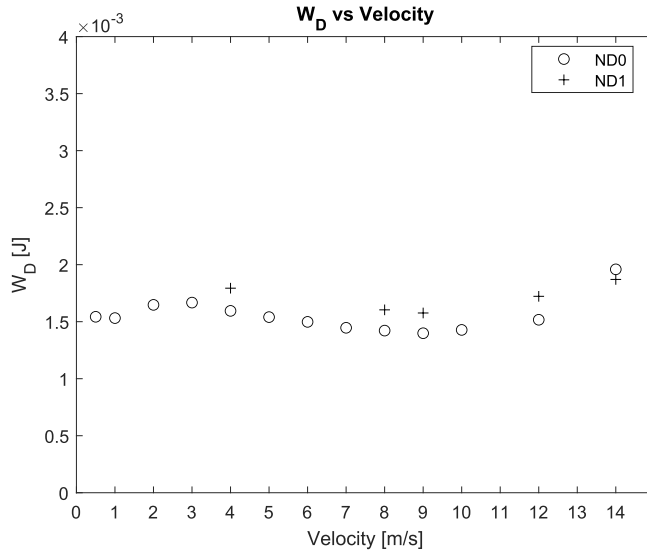


Figure 5.3: Work done by the blade on the fluid for the first mode shape of ND0 and ND1

Velocities up to 14m/s have been investigated since that value is the maximum obtainable in the testing rig.

Due to the computation time requested by the simulations, for ND1 only five values of velocity have been evaluated, but, as it is possible to see in Figure 5.3, still enough to verify the trend of the results.

5.3 Hydrodynamic damping ζ

Obtained, from the CFD simulations, the values of the work done by the hydrofoil on the fluid W_D , it has been possible to evaluate the hydrodynamic damping ζ using Equation 4.4. The operation was carried out by exporting the data as csv files and processing them with a custom MATLAB[®] code.

The results are listed in Table 5.5 and shown in Figure 5.4 and Figure 5.5, while the normalization factors, depending only on the nodal diameter, are reported in Table 5.6.

Table 5.5: Hydrodynamic damping values for ND0 and ND1 as function of the velocity

Velocity [m/s]	ζ [E-03]	
	ND0	ND1
0.5	4.6385	—
1	4.6043	—
2	4.9525	—
3	5.0125	—
4	4.7942	2.7694E+01
5	4.6300	—
6	4.5042	—
7	4.3485	—
8	4.2743	2.4762E+01
9	4.2051	2.4338E+01
10	4.2923	—
12	4.5597	2.6593E+01
14	5.8893	2.8880E+01

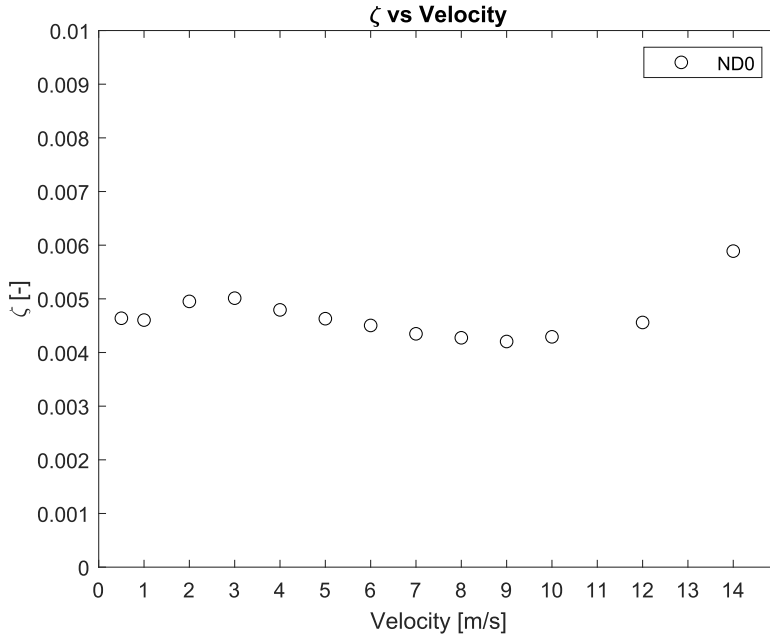
Table 5.6: Normalization factor for each nodal diameter

	Normalization factor [JE-01]
ND0	3.3264
ND1	6.4768E-01

To test the results of the CFD simulations with different boundary conditions, the first mode shape of the nodal diameter four (further in the work indicated as ND4) has been evaluated at $4m/s$. The values are reported in Table 5.7.

Table 5.7: Hydrodynamic damping value for ND4 at $4m/s$

	W_D [JE-03]	Normalization factor [JE-01]	ζ [E-02]
ND4	3.4620	2.7559	1.2562

**Figure 5.4:** Hydrodynamic damping ζ for ND0 as function of the velocity

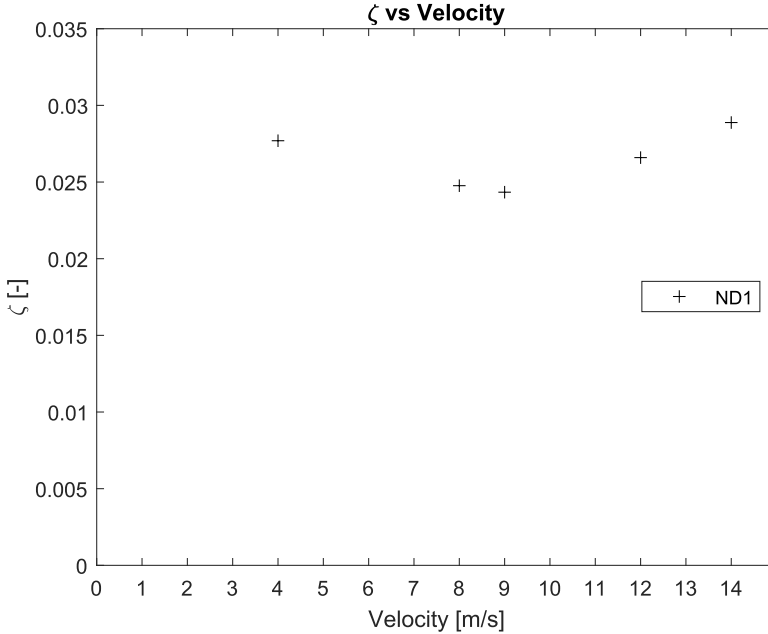


Figure 5.5: Hydrodynamic damping ζ for ND0 as function of the velocity

5.4 Discussion

A first observation regards the W_D values reported in Table 5.4 and Figure 5.3. They are all positive, so the hydrofoil is dissipating its energy in the fluid according to how the directions of the vectors in Equation 4.3 are defined. Since the normalization factor is always positive ($U \geq 0$ always) the sign of the hydrodynamic damping is determined by W_D . Resonance phenomena, indicated by negative damping values, are then not present for the tested conditions.

The trend of W_D (Figure 5.3), and so of the hydrodynamic damping ζ (Figure 5.4, Figure 5.5), matches with the one found by Bergan C., Tengs E. et. al. in [39], as it's possible to see in Figure 5.6. From previous studies, numerically conducted on the CBC at the laboratory, a lock-in velocity around $6m/s$ is expected. For lower velocities, a slightly decreasing trend was found, still in good agreement with the literature, while for velocities between $6m/s$

and 10m/s the hydrodynamic damping remains more constant. As reported in subsection 3.2.2, after the lock-in velocity is reached, the vortex shedding frequency and the one of the structure remain the same (locked-in) even if the flow velocity is increased, this can explain why the hydrodynamic damping value remains almost stable in the region just after the lock in velocity. For higher values, above 10m/s , a clear linearly increasing trend with the velocity is found, as expected.

Comparing the values of hydrodynamic damping calculated for ND0 and ND1, their difference is evident: while for ND0 $\zeta \approx 0,5\%$ for ND1 ζ is almost five times higher Figure 5.7.

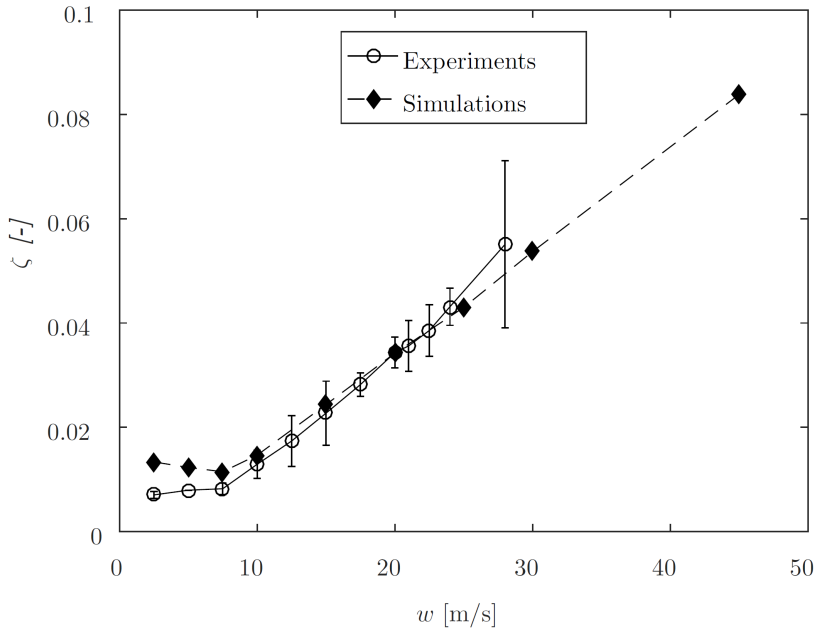


Figure 5.6: Numerical and experimental results found by Bergan C., Tengs E. et. al. for a single hydrofoil with a symmetric trailing edge [39]

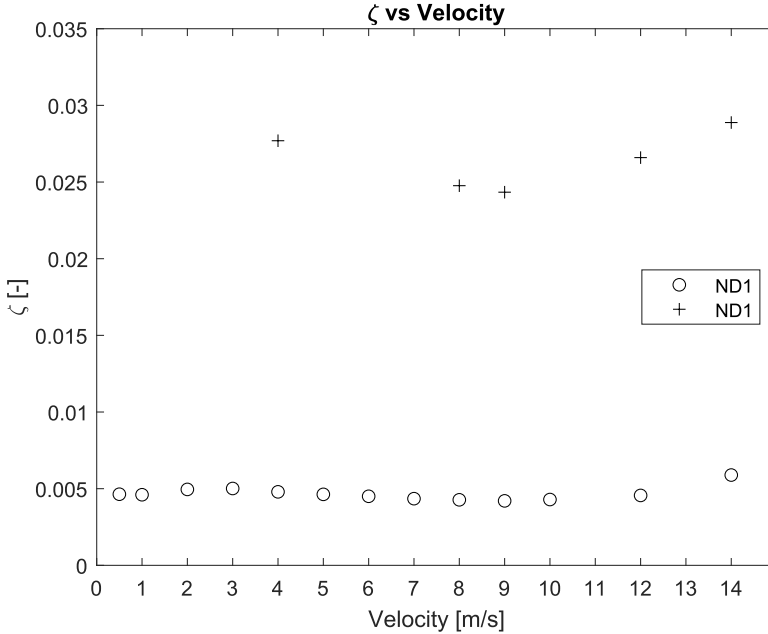


Figure 5.7: Comparison between ζ for ND0 and ND1

Previous experiments, conducted at the Waterpower laboratory on the tested geometry, showed, in condition of still water, a damping around 3% for each nodal diameter. That experimental value accounts for different contributions. As mentioned in subsection 3.4.4 the material damping, the structural damping and the viscous and hydrodynamic damping contribute to creating the damping that is measured. The separation of the contribution of each phenomenon is, experimentally, quite complex. The results for ND0 are plausible: expecting a total damping around 3% a contribution of the hydrodynamic component of approximately 0,5% is reasonable.

The values obtained for ND1 are, instead, too high to be acceptable and the reason is due to the calculation of the kinetic energy through the modal acoustic analysis. In the article of Monette et al. [14] the total potential energy U is equal to the kinetic energy that is calculated using Equation 4.2. In the equation, there are two mass contributions, one related to the structure, and the other to the water moving with the structure. Using Ansys Mechanical[®] to extract the value of kinetic energy there are no possibilities

to control how the mass of water moving with the hydrofoil is modelled. Some empirical formulas to calculate it exist, but their experimental validation is restricted to a few cases with easy geometries [40]. Another issue is related to the determination of the velocity (in Equation 4.2 represented by the product between the frequency Ω and the surface integral of the displacement). In the modal acoustic simulation, the water is still, it doesn't flow on the hydrofoil, no turbulence models are adopted and it is considered a compressible fluid. As shown in section 4.1 the component of the velocity that contributes to the kinetic energy is the one in the same direction as the deformation, that value is well estimated only for the ND0 due to its mode shape. The deformation of all the hydrofoils is the same and they move in phase (Figure 5.1), as a result, the cross-section where the fluid flows remains constant, it only changes in shape. In this configuration, if the displacement of the hydrofoil is small (less than 0,5mm) it is possible to state, with enough confidence, that the movement of the fluid in the direction of the deformation is largely due to the blade movement itself. For ND1 and all the other mode shapes where there is a variation, not only of the shape but also of the area of the cross-section where the fluid flows, the situation is different. In those cases, the water is squeezed or sucked between the hydrofoils depending if the cross-section area increases or decreases, resulting in an acceleration of the water and so in the generation of pressure gradients. This phenomenon can act on the boundary layers and on the fluid vorticity giving a non-negligible contribution to the component of the velocity needed to calculate the kinetic energy. All these effects cannot be captured with the model used in the modal acoustic simulation.

The combination of all these limitations gives, as a result, an underestimation of the value of U and so an overestimation of the hydrodynamic damping.

Some attempts have been made, trying to extract the values of velocities from the CFD simulations exposed in section 4.3 but, since their objective was different, it was not possible.

For each nodal diameter two simulations were run at 4m/s with different values of the amplitude to verify the independence of the damping from the maximum amplitude of the hydrofoil's displacement. The results, for small amplitudes (less than 0,5mm), confirm that hypothesis agreeing then with [41] and justifying the arbitrary choice of that value in the CFD simulations.

Regarding specifically the CFD simulations, a grid independence study was not performed. Nevertheless, a verification of the Courant number and y^+ for all simulations at various time steps has been performed, confirming their compliance with the recommended range for the employed models.

Chapter 6

Conclusions

The changes in the energy market due to the increasing awareness of the environment are leading to new challenges for the electric grid. The high use of renewable energy sources requires improvement in the stabilization capacity of the grid, which is usually demanded by hydroelectric power plants. Off-design operating conditions are becoming more frequent than in the past causing several failures due to fatigue phenomena.

The goal of this thesis is the numerical characterization of the hydrodynamic damping of hydrofoils in a CBC. That is the contribution to the total damping related to the flow of a fluid on the structure. Its characterization is important since it directly influences the amplitude of the displacement when the structure undergoes external dynamic loads, structural deformation decreases as the damping increases. High damping is therefore positive from a fatigue point of view.

The numerical results obtained in this master thesis agree with what was found in previous research on simpler configurations, at least for what regards the trends. A linear dependence of the work done by the hydrofoil on the fluid and so of the hydrodynamic damping is shown after the lock-in region, while before, the trend can be considered almost constant. It is then plausible to assert that the behaviour showed for simple geometries can be extended also to more complex ones like the CBC. The values of W_D extracted from the CFD simulations are consistent with each other and can therefore be considered valid, while only the results of hydrodynamic damping ζ for ND0 are plausible. For ND1 the calculated results are too high due to the underestimation of the kinetic energy computed using a modal acoustic simulation.

In summary, it is possible to assert that the adopted methodology gives

good results only for global methods where all the parts of the structure move in phase. For all different cases, where a phase angle is present and a variation of the cross-section occurs, the proposed approach is not able to model accurately the phenomenon.

The capability to determine hydrodynamic damping allows, knowing the turbine's geometry, setup, and material, to numerically estimate its vibrational behaviour, under various loading conditions. This enables the evaluation of structural responses in both design and off-design scenarios, including potential resonance phenomena. Consequently, deformations, stresses and fatigue life of the structure for different load cycles can be assessed encompassing also critical operational points. It is then possible to optimize the design, operation and maintenance strategies for both new and existing machines, aligning them with the evolving demands of a flexible energy market.

Chapter 7

Future work

A key step that still needs to be done is the experimental validation of the model on the CBC. A detailed investigation regarding the damping and how to separate the different contributions is valuable.

Finally, to obtain a model able to evaluate correct values of damping for all the nodal diameters, it would be important to extract the kinetic energy values from a suited CFD analysis.

References

- [1] Lamb, W. F., Wiedmann, T., Pongratz, J., Andrew, R., Crippa, M., Olivier, J. G. J., Wiedenhofer, D., Mattioli, G., Khourdajie, A. A., House, J., Pachauri, S., Figueroa, M., Saheb, Y., Slade, R., Hubacek, K., Sun, L., Ribeiro, S. K., Khennas, S., Can, S. d. l. R. d., Chapungu, L., Davis, S. J., Bashmakov, I., Dai, H., Dhakal, S., Tan, X., Geng, Y., Gu, B., and Minx, J., 2021, “A review of trends and drivers of greenhouse gas emissions by sector from 1990 to 2018,” [Environmental Research Letters](#), **16**(7), p. 073005, Publisher: IOP Publishing.
- [2] Matsuo, Y., Yanagisawa, A., and Yamashita, Y., 2013, “A global energy outlook to 2035 with strategic considerations for Asia and Middle East energy supply and demand interdependencies,” [Energy Strategy Reviews](#), **2**(1), pp. 79–91.
- [3] Ritchie, H., Roser, M., and Rosado, P., 2020, “CO and Greenhouse Gas Emissions,” [Our World in Data](#).
- [4] “bp Energy Outlook 2022,” .
- [5] Reynolds, T. S., 1983, *Stronger than a hundred men: a history of the vertical water wheel*, Vol. 7, JHU Press.
- [6] Francis, B. J., 2023, *Lowell hydraulic experiments*, BoD–Books on Demand.
- [7] Dixon, S. and Hall, C., 2010, “Hydraulic Turbines,” *Fluid Mechanics and Thermodynamics of Turbomachinery*, Elsevier, pp. 303–355.
- [8] Bjørsvik, E. and Faugli, P. E., 2013, “Kulturminner i norsk kraftproduksjon,” NVE, Accepted: 2018-06-07T11:03:28Z ISBN: 9788241009211

- ISSN: 1501-2832, accessed 2023-12-12, <https://nve.brage.unit.no/nve-xmlui/handle/11250/2500808>
- [9] “Statistisk årbok 2013, Tabell 19: Samlet areal, arealfordelinger og kystlinjens lengde, etter fylke. 2013,” accessed 2023-12-12, <https://www.ssb.no/a/aarbok/tab/tab-019.html>
- [10] Seidel, U., Mende, C., Hübner, B., Weber, W., and Otto, A., 2014, “Dynamic loads in Francis runners and their impact on fatigue life,” *IOP Conference Series: Earth and Environmental Science*, **22**(3), p. 032054.
- [11] Østby, P. T., Billdal, J. T., Sivertsen, K., Haugen, B., and Dahllhaug, O. G., 2016, “Dynamic stresses in high head francis turbines,” *Int. J. Hydropower Dams*, **23**(3), pp. 88–92.
- [12] Seidel, U., Hübner, B., Löfflad, J., and Faigle, P., 2012, “Evaluation of RSI-induced stresses in Francis runners,” *IOP Conference Series: Earth and Environmental Science*, **15**(5), p. 052010.
- [13] Bergan, C. W., 2019, “Dynamic Loads on Francis Turbines: An Experimental Study,” Doctoral thesis, NTNU, Accepted: 2019-05-06T12:19:18Z ISBN: 9788232637331 ISSN: 1503-8181, accessed 2023-12-26, <https://ntnuopen.ntnu.no/ntnu-xmlui/handle/11250/2596614>
- [14] Monette, C., Nennemann, B., Seeley, C., Coutu, A., and Marmont, H., 2014, “Hydro-dynamic damping theory in flowing water,” *IOP Conference Series: Earth and Environmental Science*, **22**(3), p. 032044.
- [15] Gaiti, G., “Modal analysis and characterization of a hydrofoil circular cascade test rig for hydrodynamic damping measurements,” .
- [16] Pirocca, A., “Design of an Axisymmetric Hydrofoil Cascade Test Rig,” Ph.D. thesis, Università degli Studi di Padova.
- [17] Coutu, A., Seeley, C., Monette, C., Nennemann, B., and Marmont, H., 2012, “Damping measurements in flowing water,” *IOP Conference Series: Earth and Environmental Science*, **15**, p. 2060.
- [18] Roth, S., Calmon, M., Farhat, M., Muench, C., Huebner, B., and Avelan, F., “Hydrodynamic Damping Identification from an Impulse Response of a Vibrating Blade,” .

- [19] Tengs, E. O., 2019, “Numerical simulation of Fluid-Structure Interaction in high head Francis turbines,” Doctoral thesis, NTNU, Accepted: 2019-10-29T14:28:19Z ISBN: 9788232640553 ISSN: 1503-8181, accessed 2023-12-05, <https://ntnuopen.ntnu.no/ntnu-xmlui/handle/11250/2625210>
- [20] Benra, F.-K., Dohmen, H. J., Pei, J., Schuster, S., and Wan, B., 2011, “A Comparison of One-Way and Two-Way Coupling Methods for Numerical Analysis of Fluid-Structure Interactions,” *Journal of Applied Mathematics*, **2011**, pp. 1–16.
- [21] Oftebro and Lunning, 1966, “Pressure Oscillations in Francis Turbines”. I. Oftebro - Google Search,” .
- [22] 2023, “Kármán vortex street,” Page Version ID: 1189266907, accessed 2024-01-03, https://en.wikipedia.org/w/index.php?title=K%C3%A1rm%C3%A1n_vortex_street&oldid=1189266907
- [23] “Heard_Island_Karman_vortex_street.jpg (1401×1221),” accessed 2024-01-03, https://upload.wikimedia.org/wikipedia/commons/7/71/Heard_Island_Karman_vortex_street.jpg
- [24] Schlichting, H. and Gersten, K., 2017, *Boundary-Layer Theory*, Springer Berlin Heidelberg, Berlin, Heidelberg.
- [25] Irvine, T., 1999, “KARMAN VORTEX SHEDDING AND THE STROUHAL NUMBER,” accessed 2024-01-03, <https://www.semanticscholar.org/paper/KARMAN-VORTEX-SHEDDING-AND-THE-STROUHAL-NUMBER-Irvine/181f6da07be036ac3de89e21f64ebedd28f68a90>
- [26] “Collapse-Tacoma-Narrows-Bridge-Washington-state-1940.jpg (1057×865),” accessed 2024-01-29, <https://cdn.britannica.com/21/59921-050-BCBF8853/Collapse-Tacoma-Narrows-Bridge-Washington-state-1940.jpg>
- [27] Versteeg, H. K. and Malalasekera, W., 2007, *An introduction to computational fluid dynamics: the finite volume method*, 2nd ed., Pearson/Prentice Hall, Harlow.
- [28] Young, D. F., Munson, B. R., Okiishi, T. H., and Huebsch, W. W., *A brief Introduction o Fluid Mechanics*, 5th ed., Wiley, USA.
- [29] Craig, R. and Kurdila, A., 2006, *Fundamentals of Structural Dynamics*, John Wiley & Sons.

- [30] Miner, M. A., 1945, “Cumulative Damage in Fatigue,” [Journal of Applied Mechanics](#), **12**(3), pp. A159–A164.
- [31] Zienkiewicz, O. and Taylor, R., 2000, *The Finite Element Method: Its Basis and Fundamentals - 6th Edition*, 5th ed., Vol. 1, Butterworth Heinemann.
- [32] Bedenbender, J., 2012, “English: Elastic Hysteresis,” accessed 2024-01-11, https://commons.wikimedia.org/wiki/File:Elastic_Hysteresis.svg
- [33] “Chapter 1: Introduction to Acoustic Analysis,” accessed 2024-01-12, https://ansyshelp.ansys.com/account/secured?returnurl=/account/secured?returnurl=/Views/Secured/corp/v194/ans_acous/ansacousintro.html
- [34] “A Review of Added Mass and Fluid Inertial Forces,” accessed 2024-01-15, <https://authors.library.caltech.edu/records/6819e-vnh65>
- [35] Seeley, C., Coutu, A., Monette, C., Nennemann, B., and Marmont, H., 2012, “Characterization of hydrofoil damping due to fluid–structure interaction using piezocomposite actuators,” [Smart Materials and Structures](#), **21**(3), p. 035027, Publisher: IOP Publishing.
- [36] Seeley, C., Coutu, A., Monette, C., Nennemann, B., and Marmont, H., 2013, “Determination of hydrofoil damping due to fluid structure interaction using mfc actuators,” Collection of Technical Papers - AIAA/ASME/ASCE/AHS/ASC Structures, Structural Dynamics and Materials Conference.
- [37] “SOLID187,” accessed 2024-01-14, https://www.mm.bme.hu/~gyebro/files/ans_help_v182/ans_elem/Hlp_E_SOLID187.html
- [38] “FLUID221,” accessed 2024-01-14, https://www.mm.bme.hu/~gyebro/files/ans_help_v182/ans_elem/Hlp_E_FLUID221.html
- [39] Bergan, C. W., Tengs, E. O., Solemslie, B. W., and Dahlhaug, O. G., 2019, “An Experimental Investigation of the Hydrodynamic Damping of Vibrating Hydrofoils,” **240**, Accepted: 2019-03-29T12:43:16Z Publisher: IOP Publishing.
- [40] Brennen, “A Review of Added Mass and Fluid Inertial Forces,” accessed 2023-12-21, <https://authors.library.caltech.edu/records/6819e-vnh65>

- [41] Tengs, E. O., Bergan, C. W., Jakobsen, K.-R., and Storli, P. T., 2019, “Numerical simulation of the hydrodynamic damping of a vibrating hydrofoil,” [IOP Conference Series: Earth and Environmental Science](#), **240**(6), p. 062002, Publisher: IOP Publishing.

